

Copyright
by
Mona Leila Mays
2009

The Dissertation Committee for Mona Leila Mays
certifies that this is the approved version of the following dissertation:

**The Study of Interplanetary Shocks, Geomagnetic Storms, and
Substorms with the WINDMI Model**

Committee:

Wendell Horton, Supervisor

Todd Ditmire

Richard Hazeltine

Sonia Paban

Gary Hallock

**The Study of Interplanetary Shocks, Geomagnetic Storms, and
Substorms with the WINDMI Model**

by

Mona Leila Mays, B.S.

DISSERTATION

Presented to the Faculty of the Graduate School of
The University of Texas at Austin
in Partial Fulfillment
of the Requirements
for the Degree of

DOCTOR OF PHILOSOPHY

THE UNIVERSITY OF TEXAS AT AUSTIN

August 2009

For my parents

Acknowledgments

I appreciate and thank the committee for taking the time to evaluate this work and for providing helpful comments. In particular, I sincerely thank my supervisor Professor Wendell Horton for his time, knowledge, and support. I also thank my collaborators Dr. Edmund Spencer and Professor Janet Kozyra, for their useful discussions and analysis. Thanks to Professor James Van Dam and the Institute for Fusion Studies for their support, to my mentor Dr. Chris St.Cyr, and also to Jane Pratt, Jean Perez, and Juhyung Kim for programming help and tips.

Infinite thanks go to my parents and sister Donna for everything. I am grateful to Clint for his love and support, and family Kay, Ron, Karen, and Xavier. And finally, thanks to my excellent friends Gayle, Shaun, Rebecca, Andy, Ester, Marsine, Leila R., Tim, Jadey, Conan, June, Di, and everyone I have worked with at KVRX-Austin 91.7FM.

The Study of Interplanetary Shocks, Geomagnetic Storms, and Substorms with the WINDMI Model

Publication No. _____

Mona Leila Mays, Ph.D.

The University of Texas at Austin, 2009

Supervisor: Wendell Horton

WINDMI is a low dimensional plasma physics-based model of the coupled magnetosphere-ionosphere system. The nonlinear system of ordinary differential equations describes the energy balance between the basic nightside components of the system using the solar wind driving voltage as input. Of the eight dynamical variables determined by the model, the region 1 field aligned current and ring current energy is compared to the westward auroral electrojet AL index and equatorial geomagnetic disturbance storm time Dst index. The WINDMI model is used to analyze the magnetosphere-ionosphere system during major geomagnetic storms and substorms which are community campaign events. Numerical experiments using the WINDMI model are also used to assess the question of how much interplanetary shock events contribute to the geoeffectiveness of solar wind drivers. For two major geomagnetic storm intervals, it is found that the magnetic field compressional jump is important to producing the changes in the AL index. Further, the WINDMI

model is implemented to compute model AL and Dst predictions every ten minutes using real-time solar wind data from the ACE satellite as input. Real-Time WINDMI has been capturing substorm and storm activity, as characterized by the AL and Dst indices, reliably since February 2006 and is validated by comparison with ground-based measurements of the indices. Model results are compared for three different candidate input solar wind driving voltage formulas. Modeling of the Dst index is further developed to include the additional physical processes of tail current increases and sudden commencement. A new model, based on WINDMI, is developed using the dayside magnetopause and magnetosphere current systems to model the magnetopause boundary motion and the dayside region 1 field aligned current which is comparable to the auroral upper AU index.

Table of Contents

Acknowledgments	v
Abstract	vi
List of Tables	xi
List of Figures	xii
Chapter 1. Solar Wind-Magnetosphere Interactions	1
1.1 Solar Wind	1
1.1.1 Coronal Mass Ejections	2
1.1.2 Interplanetary Shocks	3
1.2 Solar Wind - Magnetosphere Coupling	4
1.3 Plasma Flows in the Magnetosphere	6
1.4 Magnetic Field Configuration and Plasma Populations	7
1.4.1 Intrinsic Dipole Field	7
1.4.2 Chapman-Ferraro and Magnetopause Currents	8
1.4.3 Magnetotail Current and Lobes	11
1.4.4 Ring Current	12
1.4.5 Region 1 and Region 2 Field-Aligned Currents	14
1.5 Magnetospheric Dynamics	19
1.5.1 Geomagnetic Storms	20
1.5.2 Geomagnetic Substorms	21
1.5.3 Geomagnetic Indices	21
Chapter 2. WINDMI Model	24
2.1 Description	24
2.2 WINDMI Development	25
2.3 WINDMI Differential Equations	26

2.4	WINDMI Parameters	28
2.5	WINDMI Input	29
2.5.1	Solar Wind Data from ACE	29
2.5.2	Solar Wind-Magnetosphere Coupling Functions	32
Chapter 3.	Effect of Interplanetary Shocks on the <i>AL</i> and <i>Dst</i> Indices	35
3.1	Introduction and Methodology	35
3.2	Analytic ACE Data	36
3.3	Event Descriptions and WINDMI Analysis	38
3.3.1	15-24 April 2002	38
3.3.2	3-6 October 2000	43
3.4	Conclusions	44
Chapter 4.	Real-Time WINDMI Model	47
4.1	Introduction	47
4.2	Real-Time WINDMI	48
4.3	Measures of Performance	49
4.4	Real-Time WINDMI Results: February 2006 - August 2008	50
4.4.1	Event Selection	50
4.4.2	Model Performance	51
4.5	Real-Time WINDMI Results: 14-18 December 2006	56
4.6	Discussion and Conclusions	61
Chapter 5.	Dayside WINDMI Model	66
5.1	Introduction	66
5.2	Dayside Magnetopause Dynamics	67
5.3	Sudden Storm Commencement	74
5.4	Tail Current Contribution to the <i>Dst</i>	75
5.5	Improved <i>Dst</i> Modeling	75
5.6	Dayside WINDMI Model	76
5.7	Discussion	79
Chapter 6.	Conclusions	81

Appendix	85
Appendix 1. Geophysical Coordinate Systems	86
1.1 Geomagnetic Coordinates (MAG)	86
1.2 Geocentric Solar Magnetospheric Coordinates (GSM)	86
Bibliography	87
Vita	98

List of Tables

2.1	WINDMI Nominal Parameters, estimated by physical considerations of the state and geometry of the nightside magnetosphere using the Tsyganenko magnetic field model[55].	30
2.2	WINDMI Nominal Parameters, estimated by physical considerations of the state and geometry of the nightside magnetosphere using the Tsyganenko magnetic field model.	31
3.1	A listing of observed ACE IP Shock dates, times, and calculated speeds (assuming a parallel shock) during 15-24 April 2002, with associated SOHO CME times and speeds. Dates of observed magnetic cloud structure in ACE IMF B_y , B_z , and clock angle are also listed.	41
4.1	The list of 22 events for which storms and/or substorms have been predicted by Real-Time WINDMI from February 2006 to August 2008. The WDC Kyoto minimum Dst and AL data for each event are given in the first two columns.	52
4.2	Mean Average Relative Variance (ARV) measures of Real-Time WINDMI model results with the AL and Dst index are shown in the second and third columns. for the selected events from February 2006 - August 2008 (listed in Table 4.1). The ARV is calculated using Equation 4.1 in Section 4.3.	53
4.3	Mean correlation coefficient (COR) of Real-Time WINDMI model results with the AL index are shown in the second column and with the Dst index in the fourth column. The third column shows the mean direct correlation between the calculated input driving voltage V_{sw} and the AL index. The COR is calculated using Equation 4.2 in Section 4.3.	53
4.4	Mean values of the Root Mean Squared Error (RMSE) of Real-Time WINDMI model results with the AL and Dst index are shown in the second and third columns. The RMSE is calculated using Equation 4.3 in Section 4.3.	55
5.1	WINDMI dayside parameters for the $(R_{mp}(t), v_{mp}(t))$ system (Equations 5.9 and 5.10).	71
5.2	Dayside WINDMI parameters of Equations 5.20-5.25, estimated by physical considerations of a typical state and geometry of the dayside magnetosphere.	79

List of Figures

1.1	Magnetosphere.	9
1.2	Magnetosphere currents.	10
1.3	Nightside current systems as viewed along the Sun-Earth line.	16
1.4	Typical patterns of the region 1 and region 2 currents in the ionosphere as viewed from the North Pole.	17
1.5	Substorm current wedge.	18
2.1	WINDMI model geometry of five energy regions (1) the magnetotail lobe with current $I(t)$, (2) central plasma sheet with pressure p and kinetic energy K_{\parallel} (not shown), (3) the ring current I_{rc} with energy W_{rc} and A_{eff} effective aperture for particle injection into the ring current, (4) the nightside region 1 current $I_1(t)$, and (5) the portion of the nightside region 2 current closing as the partial ring current $I_2(t)$	25
3.1	The bottom panel shows the ACE data for the solar wind $B_{\perp} = (B_y^2 + B_z^2)^{1/2}$ during the April 2002 storm. The top panel shows the analytic parameter for the solar wind B_{\perp} for which certain shock/sheath features have been removed from the analytic shock field based on the ACE data.	37
3.2	Top panels: ACE solar wind data for 15-24 April 2002 in GSM coordinates showing the interplanetary magnetic field components B_y and B_z , proton number density n_{sw} , and solar wind flow velocity $u_x(t)$. Three interplanetary shocks are identified by S1, S2, S3 occurring at 1020 UT 17 April, 0801 UT 19 April, and 0414 UT 23 April. Bottom panels: The corresponding time advanced AL and Dst data during this period shows substorm (shaded) and storm activity.	39
3.3	WINDMI results for V_{sw} input derived from solar wind parameter data or analytic parameters for which all three shock/sheath features have been removed from B_{\perp} . The analytic shock field B_{\perp} without the shock/sheath features (top panel of Figure 3.1), and ACE data for the u_{sw} and n_{sw} parameters was used to derive the input solar wind dynamo voltage shown in the top panel. WINDMI $-AL$ and Dst results for this input are shown in the middle and bottom panels (dashed lines), respectively. decrease of 50% in the three AL peaks times and there is	42

4.1	ACE solar wind number density, velocity, and interplanetary magnetic field data for 14-18 December 2006 in GSM coordinates show a shock at 1352 UT on 14 December with a speed of 1030 km/s. . . .	57
4.2	Rectified V_{sw}^{Bs} (blue), Siscoe V_{sw}^S (red), and Newell V_{sw}^N (green) input solar wind driving voltages for 14-18 December 2006.	58
4.3	Real-time WINDMI AL and Dst results for 14-18 December 2006. Model results using as input the Rectified voltage V_{sw}^{Bs} are shown in blue, the Siscoe voltage V_{sw}^S in red, and Newell voltage V_{sw}^N in green. WDC Kyoto provisional AL and Dst data is shown in black, and the SYM-H data in gray.	59
4.4	Magnetopause standoff distance R_{mp} computed using the Shue et al. [42] equation and ACE data for 14-18 December 2006	60
4.5	Zoom in on magnetopause standoff distance shown in Figure 4.4 for 14 December. The shock times at ACE are marked by dotted red lines and the AL spikes by solid red lines. The first AL spike not captured by WINDMI is thought to be a result of the sudden dayside compression associated with shock arrival.	62
4.6	AL and AU data for 15 December with AL spikes marked by solid red lines with values -2191 nT, -2349 nT, -2237 nT, and -2183 nT at 0246 UT, 0324 UT, 0852 UT, and 1135 UT.	63
5.1	ACE solar wind number density, velocity, and interplanetary magnetic field data for 19-23 November 2007 in GSM coordinates.	72
5.2	19-23 November 2007: The dynamics of Equations 5.9 and 5.10 for the magnetopause shell at $R_{mp}(t)$ and the radial velocity $v_r(t) = dR_{mp}(t)/dt$	73
5.3	Dayside view along the Sun-Earth line of the geometry of the region 1 (R1), region 2 (R2), ring current (RC), and magnetopause current loops corresponding to the nightside current systems shown in Figure 1.3. I_1^d is taken to be proportional to the eastward auroral electrojet. The northward electric field drives a Hall current eastward contributing strongly to the eastward electrojet. The eastward electrojet give the AU geomagnetic index.	78

Chapter 1

Solar Wind-Magnetosphere Interactions

1.1 Solar Wind

The gas pressure difference between the solar corona and interstellar space creates the solar wind which streams outward at around 450 km/s (at 1 AU) and this can vary from 200 km/s to 1000 km/s. At the Sun, the typical solar wind speed distribution during solar minimum varies from 750 to 800 km/s at the solar poles where large coronal holes are often located, to the slow solar wind at 300 to 400 km/s at lower heliographic latitudes[37]. The plasma expands supersonically from the hot corona in which ion-electron collisions are frequent, to the cool and low-dense interplanetary plasma in which collisions are rare with a collisional mean free path of about 1 AU (1.5×10^{11} m). Changes in the solar magnetic field significantly influence the behavior of the solar wind. The properties of the solar wind are continuously measured by space probes just upstream of the Earth. At 1 AU it is comprised mostly of ionized hydrogen and carries out a frozen-in magnetic field with a fixed source that differentially rotates with the Sun. The resulting magnetic field line pattern is known as the Parker spiral and at the Earth the interplanetary magnetic field (IMF) value is about 7×10^{-9} T, in the ecliptic plane and at 45 degrees to the Sun-Earth line. At 1 AU the average solar wind densities are 6.6 cm^{-3} protons, 7.1 cm^{-3} electrons, and 0.25 cm^{-3} of doubly ionized helium. The proton temperature

is 1.2×10^5 K (10 eV) and electron temperature 1.4×10^5 K (12 eV)[23]. At these low densities the 10 eV hydrogen gas is fully ionized as follows from the Saha equation.

1.1.1 Coronal Mass Ejections

Coronal mass ejections (CMEs), which are ejections of hot plasma from large regions of the corona, inject plasma and energy into the solar wind and often have associated interplanetary shocks. The plasma in the corona is highly conducting and because Sun's magnetic field is frozen into the plasma the tops of the closed field lines must be carried away from the Sun along with the ejected plasma. This causes the field lines to become stretched into long loops extending into interplanetary space and the solar source region becomes magnetically open. CMEs can be observed in the visible light spectrum with coronagraphs and were first discovered with coronagraphs on spacecrafts in the early 1970s. White-light coronagraphs detect photospheric light which has been Thomson-scattered off free electrons in the corona. The radiation recorded at a point in a coronagraph image is a line of sight integral of the light scattered along the entire path extending through the corona to the observer or instrument. The true three-dimensional CME electron density structure is projected onto a two-dimensional image. Halo CMEs are directed completely away from, or towards the Earth and form a "halo" of bright material in the coronagraph images and the Earth-directed Halo CMEs often trigger geomagnetic storms. The speeds of CMEs are measured by tracking the projection of the CME leading edge feature onto the plane of the sky in a time sequence of coronagraph images. Plasma, particle and magnetic properties of CMEs can be measured in situ and they can be detected

remotely in the X-ray, EUV, H α , and radio parts of the spectrum[19].

Interplanetary coronal mass ejections (ICMEs) originate as coronal mass ejections at the Sun and are observed in situ as enhanced magnetic structures in the solar wind lasting on the order of a day[64]. Magnetic clouds (MCs) are a subclass of ICMEs with above-average strength magnetic fields which rotate smoothly through a large angle in a low beta plasma.

1.1.2 Interplanetary Shocks

Interplanetary (IP) shocks are traveling collisionless shocks which propagate out through the heliosphere. IP shocks and their resulting geomagnetic activity are usually caused by Halo ICMEs and their associated dynamic interaction regions, also known as “sheath regions”[13]. These sheath regions are accelerated due to the momentum exchange from the fast CME, and they have enhanced densities and temperatures, since they have interacted with the shock. Collisionless shocks can also be formed at the interface of corotating interaction regions (CIRs) in which a slow solar wind stream is overtaken by a fast stream which usually originate from coronal holes[47, 54]. It is still not well understood how interplanetary structures such as the CMEs, shocks, density fluctuations, and corotating interaction regions propagate in the inner heliosphere.

The conservation of mass, energy, and momentum in collisionless shocks and using MHD, gives the shock-jump or Rankine-Hugoniot relations which relate the upstream and downstream plasmas. However, unlike in collisional gases, the downstream state is not uniquely determined by the upstream parameters without

knowing additional information about the shock structure. The shock-jump conditions are

$$[\rho \mathbf{u} \cdot \hat{\mathbf{n}}]_1^2 = 0 \quad (1.1)$$

$$[\rho \mathbf{u}(\mathbf{u} \cdot \hat{\mathbf{n}}) + (P + B^2/2\mu_0)\hat{\mathbf{n}} - (\mathbf{B} \cdot \hat{\mathbf{n}})\mathbf{B}/\mu_0]_1^2 = 0 \quad (1.2)$$

$$[\mathbf{u} \cdot \hat{\mathbf{n}}(\rho I + \rho u^2/2 + B^2/2\mu_0) + (P + B^2/2\mu_0) - (\mathbf{B} \cdot \hat{\mathbf{n}})(\mathbf{B} \cdot \hat{\mathbf{u}})\mathbf{B}/\mu_0]_1^2 = 0 \quad (1.3)$$

$$[\mathbf{B} \cdot \hat{\mathbf{n}}]_1^2 = 0 \quad (1.4)$$

$$[\hat{\mathbf{n}} \times (\mathbf{u} \times \mathbf{B})]_1^2 = 0. \quad (1.5)$$

These shock-jump conditions apply to steady state plasma flows with sharp jumps in the fields. In simulations shocks with $\beta_i \approx 1$ and larger Alfvén mach numbers are not steady but show large fluctuations. There is a critical Mach number above which there are kinetic effects giving energy and momentum transfer beyond the scope of MHD description.

1.2 Solar Wind - Magnetosphere Coupling

The Sun is a magnetically-variable star, and there are consequences for planets with either intrinsic magnetic fields or atmospheres, or with both like Earth. It is the powerful, dominant driver of activity in the inner heliosphere including the geospace environment. It takes 3 to 4 days for the solar wind to flow to the Earth where it has a dynamic pressure (radial momentum flux) of about 3×10^{-9} P and is mostly carried by protons. The sound speed in the upstream plasma is about

60 km/s which is comparable to the Alfvén speed of 40 km/s. The supersonic, low density solar wind plasma forms a fast magnetosonic shock front at around $14 R_E$ ($1 R_E = 6.378137 \times 10^6$ m), called the bow shock, just in front of the magnetosheath which contains subsonic, high density plasma. The collisional mean free path in the bow shock is about 100 to 1000 km. (Geosynchronous orbit is around $6.6 R_E$). Thin surface current sheets on the magnetopause separate the geomagnetic field and terrestrial plasmas from the solar wind plasma and interplanetary magnetic field. The Earth’s magnetic field is an obstacle in the solar wind plasma and the shape of the magnetosphere is determined by the balance of the solar wind dynamic pressure and the Earth’s magnetic pressure at every point on the boundary. The magnetospheric cavity is compressed at the dayside and forms a long tail along the Sun-Earth line which acts as a reservoir of plasma and energy.

In the polar regions plasma flows noon to midnight and then has a sunward flow back to the dayside at slightly lower latitudes, creating a double vortex pattern on the dawn and dusk sides of the polar cap. This pattern is termed *magnetospheric convection* although it is not at all thermally driven. Here the plasma flow is driven by the $\mathbf{E} \times \mathbf{B}$ drift that is large compared to the diamagnetic pressure gradient flow velocities. The positive and negative charged centers of the vortex pattern and associated strong electric fields are driven by the solar wind dynamo during periods of southward IMF. Dungey [9] showed that this magnetospheric convection pattern could be produced by the reconnection of interplanetary and geomagnetic field lines on the dayside magnetopause such that two types of field lines develop. Each field line will have one end attached near the north or south pole while the other ends

will be stretched out in interplanetary space. The solar wind flow with frozen-in flux pulls the interplanetary part of the field lines antisunward. Thus the mapping of these convecting field lines is from noon towards midnight in the ionosphere. The flux is returned by another reconnection between these two north and south open field lines occurring at the x-line in the geomagnetic tail and the newly formed geomagnetic field line will flow Earthward.

1.3 Plasma Flows in the Magnetosphere

A proton in the magnetosphere experiences three types of motion (1) gyromotion about the magnetic field lines, (2) bounce motion along the field lines, and (3) drift perpendicular to field lines.

The particle drift motion perpendicular to the magnetic field arises from the $\mathbf{E} \times \mathbf{B}$ drift, gradient drift, and curvature drift. In a dipole field the gradient and curvature drifts give rise to motion in the same direction because the radius of curvature and magnetic field gradient are in opposite directions.

In addition, the dawn to dusk electric field causes particles to drift toward the sun, and the corotation electric field causes particles to rotate eastward with the Earth. Depending on charge, energy, and distance from the Earth, this trapped particle region can be calculated. In the equatorial plane, the Alfvén layer defines the separatrix between particle trajectories that lead from the magnetotail to the dayside magnetopause and those are trapped to circle the Earth.

1.4 Magnetic Field Configuration and Plasma Populations

1.4.1 Intrinsic Dipole Field

The Earth's magnetic field in the inner magnetosphere can be approximated as a pure dipole field. In local spherical polar coordinates (see Appendix 1) the covariant vector potential for the magnetic field is

$$\begin{aligned}\mathbf{A}_{\text{dip}} &= \frac{M_{\text{dip}} \sin\theta}{r^2} \hat{\mathbf{e}}_\phi = \frac{M_{\text{dip}} \sin\theta}{r^2} (\nabla\phi \ r \sin\theta) \\ &= \frac{M_{\text{dip}} \sin^2\theta}{r} \nabla\phi = \Psi \nabla\phi.\end{aligned}\tag{1.6}$$

The Earth's dipole moment \mathbf{M}_{dip} is around $8 \times 10^{15} \text{ T} \cdot \text{m}^3$ and is tilted about 11° to the rotation axis[23]. The flux function is Ψ_{dip} is

$$\Psi_{\text{dip}} = \frac{M_{\text{dip}} \sin^2\theta}{r} = \frac{B_0 R_E^3 \sin^2\theta}{r},\tag{1.7}$$

where B_0 is the equatorial surface field and averages around 30,438 nT. The gradient of the flux function Ψ_{dip} is

$$\nabla\Psi_{\text{dp}} = \frac{B_0 R_E^3 \hat{\mathbf{e}}_r \sin^2\theta}{-r^2} + \frac{B_0 R_E^3 \hat{\mathbf{e}}_\theta 2\sin\theta \cos\theta}{r^2}\tag{1.8}$$

$$= \frac{-B_0 R_E^3 \sin\theta (1 + 3\cos^2\theta)^{1/2}}{r^2} \hat{\mathbf{n}}(\theta)\tag{1.9}$$

where $\hat{\mathbf{n}}(\theta) = (\sin\theta \hat{\mathbf{e}}_r - 2\cos\theta \hat{\mathbf{e}}_\theta) / (1 + 3\cos^2\theta)^{1/2}$ is the unit normal to the undisturbed magnetosphere surface. The magnetic field from the vector potential is

$$\mathbf{B}_{\text{dip}} = \nabla \times \mathbf{A}_{\text{dip}} = \frac{\mu_0}{4\pi} \left[\frac{3\mathbf{n}(\mathbf{n} \cdot \mathbf{M}_{\text{dip}}) - \mathbf{M}_{\text{dip}}}{\mathbf{r}^3} \right]\tag{1.10}$$

which can be written in component form as

$$\mathbf{B} = \nabla\Psi_{\text{dp}} \times \nabla\phi = \frac{B_0 R_E^3 (2\cos\theta\hat{\mathbf{e}}_r + \sin\theta\hat{\mathbf{e}}_\theta)}{r^3}. \quad (1.11)$$

However, the actual magnetospheric configuration has a day-night asymmetry from the pure dipole due to the solar wind dynamic pressure. The Earth's magnetosphere can be expressed as the sum of the contributions from the field produced by (1) currents in the liquid core $\mathbf{B}_{\text{dip}}(\mathbf{M}_{\text{dip}})$, (2) the tail current $\mathbf{B}_{\text{tail}}(I_{\text{tail}})$ (3) the ring current $B_{\text{rc}}(I_{\text{rc}})$ (4) the Chapman-Ferraro (CF) current loops $\mathbf{B}_{\text{CF}}(I_{\text{CF}})$, (5) the region 1 field-aligned current loops $\mathbf{B}_1(I_1)$, and (6) the region 2 field aligned current (FAC) loops $\mathbf{B}_2(I_2)$.

1.4.2 Chapman-Ferraro and Magnetopause Currents

The role of the magnetopause current is to confine the Earth's field to the magnetosphere. This current has the effect of increasing the magnetic field everywhere inside the magnetopause. The Chapman-Ferraro current system consists of dayside current loops which close completely on the magnetopause. Near the equatorial plane, the flow is primarily in the eastward direction such that there is a northward magnetic perturbation $\Delta\mathbf{B}_{\text{CF}}$ in the magnetosphere thereby increasing the magnetic field at the Earth's surface.

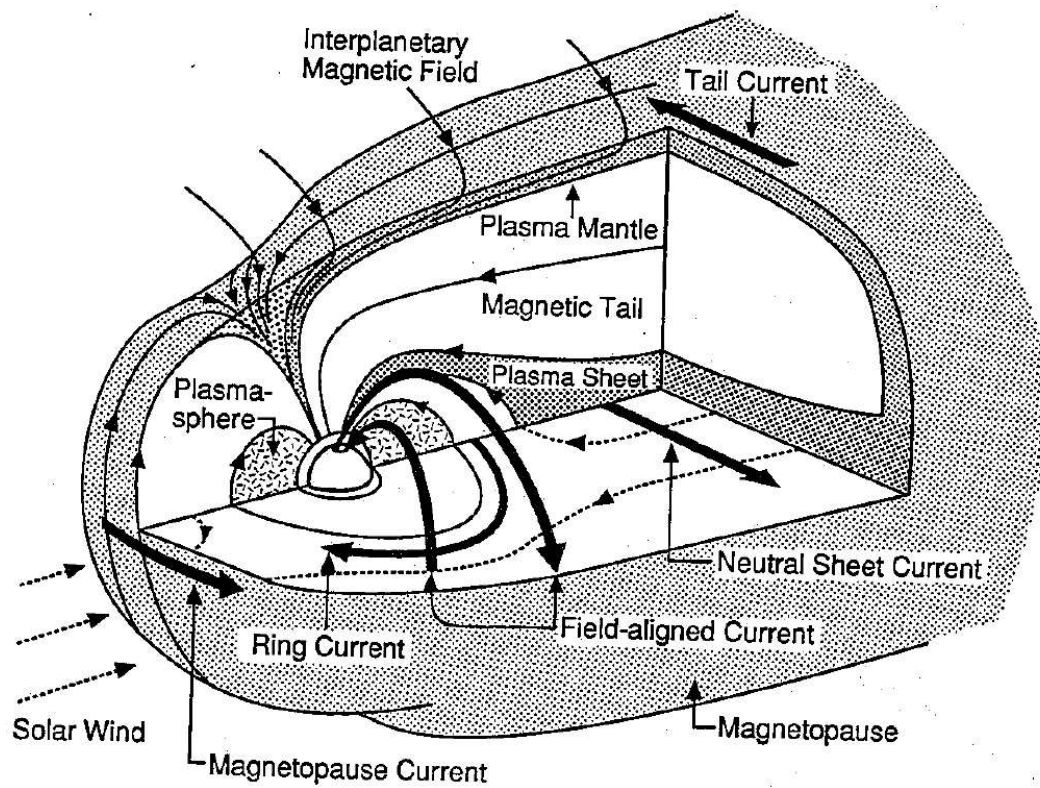


Figure 1.1: Magnetosphere.

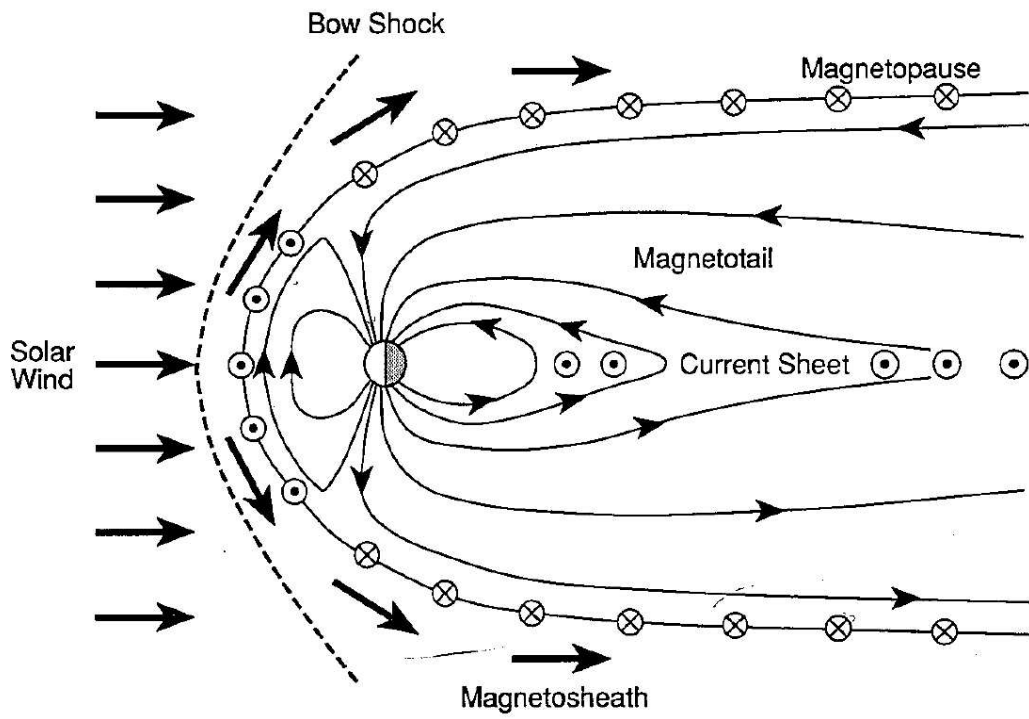


Figure 1.2: Magnetosphere currents.

During southward IMF the subsolar reconnection current system forms closed equatorial loops that connect the magnetopause with the bow shock. On the magnetopause surface, this current system flows in the same sense as the Chapman-Ferraro current. For northward IMF, magnetic reconnection occurs tailward of the polar entry cusps giving the polar reconnection current system which forms closed loops that connect the magnetopause with the bow shock[44]. The magnetopause segment of this system flows in same sense as the Chapman-Ferraro current system in the polar regions but does not contribute any magnetopause surface currents in the equatorial plane.

1.4.3 Magnetotail Current and Lobes

Earth's field lines are dragged antisunward through tangential stresses between the solar wind and Earth's magnetic field producing the magnetotail. The geomagnetic tail is the largest reservoir of plasma and energy in the magnetosphere. The tail current sheet, or central plasma sheet (CPS) is a region of hot plasma which separates the anti-sunward and sunward magnetic fields in the geomagnetic tail lobes and flows in the same direction as the ring current in the midnight equatorial plane which reduces the magnetic field at the Earth's surface. The high energy of $T_e \approx 0.6$ keV, $T_i \approx 4.2$ keV, and density $n_{cps} \approx 0.3$ cm⁻³ central plasma sheet is formed by the $\mathbf{E} \times \mathbf{B}$ drift of magnetotail plasma and has an approximate pressure of 0.25 nPa. The magnetic field in the tail lobes is around 20 nT and the magnetic pressure is much higher than the particle pressure. The magnetic flux from each tail lobe maps directly to each of the polar caps. The polar caps are the areas around

each magnetic pole bounded by the auroral ovals, which are the boundaries between field lines which close entirely in the magnetosphere and field lines that close on the magnetopause.

The cross-tail current in the central plasma sheet closes on the magnetopause such that the tail current forms a theta pattern when viewed along the Sun-Earth line. About 10^6 A of current is carried in each $5 R_E$ section of the tail for total stored energy of 10^{15} J. The plasma in the geomagnetic tail has a structure similar to the laboratory theta-pinch with a plasma current of approximately 20 MA trapping a high pressure plasma sheet. The nonlinear structure is rather stable and continuous for energies on the order of $W_{\text{tail}} \approx 10^{15}$ J. There must be a pressure equilibrium between the solar wind pressure, the magnetic pressure in the lobes, and the thermal plasma sheet pressure. The tail radius increases, or flares, as the distance down the tail increases and then reaches an asymptotic radius of around $30 R_E$ at around $150 R_E$ down the tail. However, the geometry of the geomagnetic tail this distance down the tail is highly variable and dependent on solar wind conditions. The lunar orbit which is around $60 R_E$ crosses the geomagnetic tail.

1.4.4 Ring Current

The radiation belts are made up of particles which orbit the Earth from about $1.6 R_E$ to $6 R_E$ and the particles with the higher energies and number densities orbit near the equatorial plane. All trapped radiation belt particles contribute to the ring current, however ring current usually refers to the components of the particle distribution which contribute to the total current density. The current is produced

by gradient and curvature drifting particles in the radiation belts. The Van Allen belts refers to particles, mostly electrons, that have penetrating radiation.

Dessler and Parker [7], and Sckopke [41] showed that the change in the magnetic field at the Earth's surface is an indication of the total plasma energy of the ring current particles. At low latitudes the ring current effectively reduces the horizontal component of the surface magnetic field. Assuming a nonconducting Earth, the change in the magnetic field at the center of the Earth due to the ring current ΔB_{rc} arises from three types of motion of the trapped particles. There is the 1) charge dependent gradient drift, 2) curvature drift and 3) gyromotion of the plasma particles.

$$\mathbf{v}_{\text{grad drift}} = \frac{1}{2}mv_{\perp}^2 \frac{\mathbf{B} \times \nabla \mathbf{B}}{qB^3} \quad (1.12)$$

$$\mathbf{v}_{\text{curvature drift}} = mv_{\parallel}^2 \frac{\mathbf{B} \times (\mathbf{B} \cdot \nabla) \mathbf{B}}{qB^4} \quad (1.13)$$

Because the dipole field is a vacuum field with $\nabla \times \mathbf{B}_{\text{dip}} = 0$ the term $(\mathbf{B} \cdot \nabla) \mathbf{B}$ becomes $B \nabla_{\perp} \mathbf{B}$. The two drifts combine and the current density from the drifts is

$$\begin{aligned} \mathbf{J}_{\text{drift}} = qn(\mathbf{v}_{\text{grad}} + \mathbf{v}_{\text{curv}}) &= \left(\frac{1}{2}mv_{\perp}^2 + mv_{\parallel}^2 \right) \frac{\mathbf{B} \times \nabla \mathbf{B}}{B^3} \\ &= (P_{\perp} + P_{\parallel}) \frac{\mathbf{B} \times \nabla \mathbf{B}}{B^3}. \end{aligned} \quad (1.14)$$

The component of the Earth's magnetic field in the equatorial plane from

Equation 1.11 is used to obtain

$$\mathbf{J}_{\text{drift}} = - (P_{\perp} + P_{\parallel}) \frac{3R^2}{B_0 R_E} \hat{\mathbf{e}}_{\theta}. \quad (1.15)$$

The magnetic field at the center of the Earth due to particle drifts in the equatorial plane is

$$\Delta \mathbf{B}_{\text{drift}} = -\frac{\mu_0}{4\pi} W \frac{3R^2}{B_0 R_E^3} \hat{\mathbf{e}}_z. \quad (1.16)$$

The particle gyromotion around the magnetic field spreads the magnetic field locally which produces a change in the magnetic field outside the orbit from the magnetic dipole moment $\boldsymbol{\mu} = -1/2 m v_{\perp}^2 \hat{\mathbf{e}}_z / B_E$

$$\Delta \mathbf{B}_{\text{moment}} = \frac{\mu_0}{4\pi} \frac{W_{\perp}}{B_0 R_E^3} \hat{\mathbf{e}}_z, \quad (1.17)$$

where $W_{\perp} = \mu B$. The total magnetic field at the center of the earth produced by the ring current is

$$\begin{aligned} \Delta \mathbf{B}_{\text{rc}} &= \Delta \mathbf{B}_{\text{drifts}} + \Delta \mathbf{B}_{\text{moment}} \\ &= -\frac{\mu_0}{2\pi} \frac{W_{\text{rc}}(t)}{B_E R_E^3} \hat{\mathbf{e}}_z. \end{aligned} \quad (1.18)$$

This Equation is known as the Dessler-Parker-Sckopke relation.

1.4.5 Region 1 and Region 2 Field-Aligned Currents

A schematic of the nightside current systems as viewed along the Sun-Earth line are shown in Figure 1.3. The magnetic field in the stretched tail must map to the polar and auroral ionospheres, therefore magnetospheric flows must drive the plasma flows in the ionosphere (see Section 1.4.3). This is achieved through the

Birkeland field-aligned currents of which the region 1 field-aligned currents flow into the ionosphere from the dawn side and out from the dusk side at higher latitudes and closes in the opposite sense as the ring current in the equatorial plane. At lower latitudes the region 2 currents flow into the ionosphere on the dusk side and out from the dawn side, and closes in the same sense as the ring current in the equatorial plane. The partial ring current is located in the dusk region and flows in the same sense as the ring current in the equatorial plane and then closes in the ionosphere from noon to midnight, connecting to the field-aligned currents. The ionospheric portions of the field aligned currents are called the auroral electrojets, with the region 1 current closing as the westward electrojet in the E-layer (≈ 90 -120 km) and the region 2 current as the eastward electrojet. Typical patterns of the region 1 and region 2 currents in the ionosphere as viewed from the North Pole are shown in Figure 1.4.

As discussed in Section 1.4.3, the central plasma sheet carries a considerable cross-tail current and only a small diversion of part of this current is sufficient to increase the region 1 field aligned current, and associated auroral electrojet currents as observed in the ionosphere. A sketch of the tail current diversion geometry known as the substorm current wedge is shown in Figure 1.5.

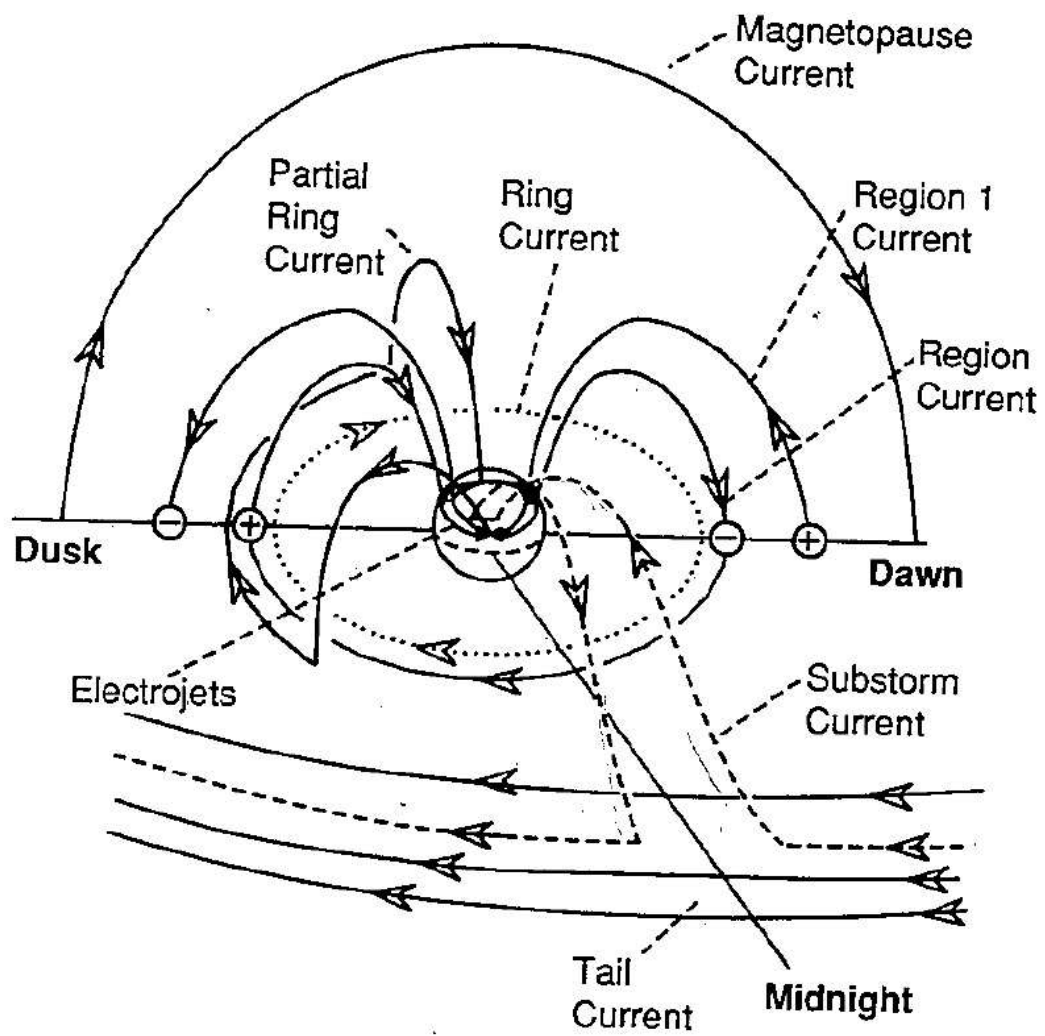


Figure 1.3: Nightside current systems as viewed along the Sun-Earth line.

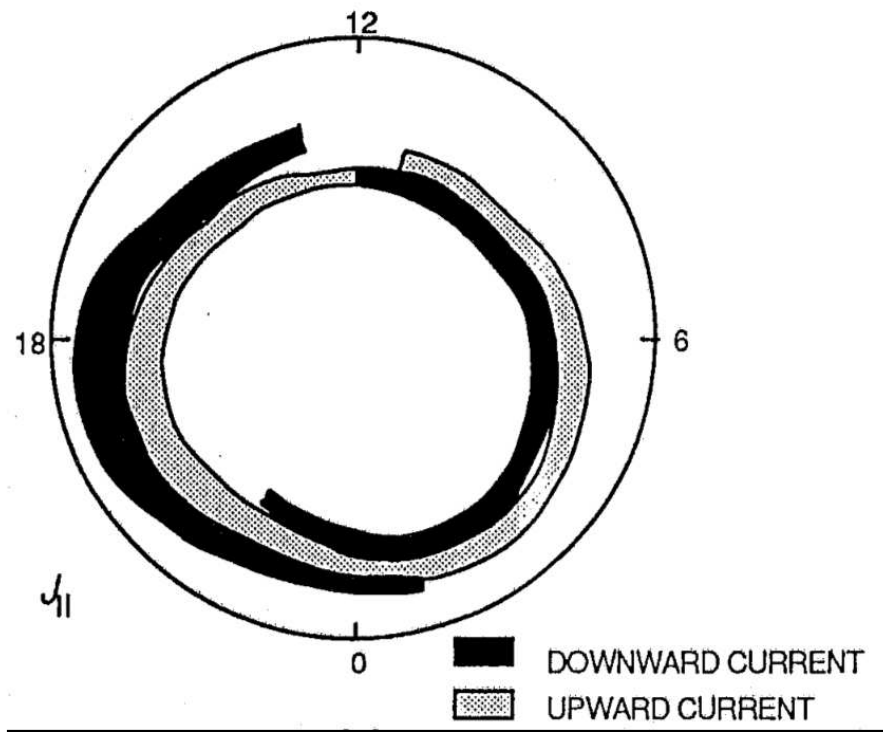


Figure 1.4: Typical patterns of the region 1 and region 2 currents in the ionosphere as viewed from the North Pole.

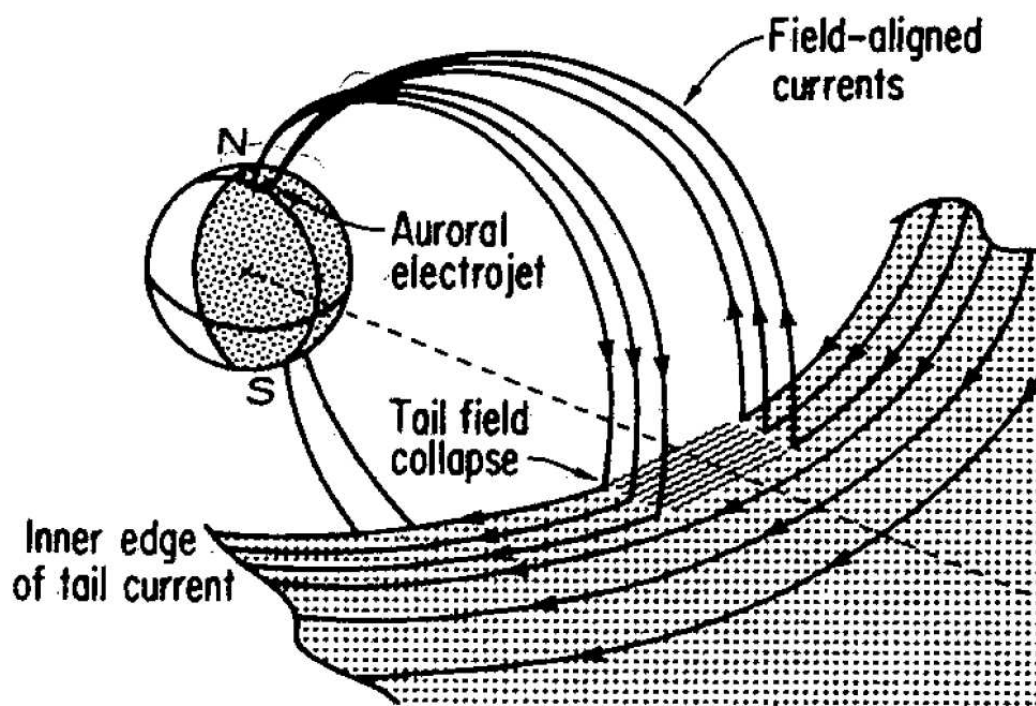


Figure 1.5: Substorm current wedge.

In the ionosphere collisions between charged particles and the neutral atmosphere creates a high conductivity perpendicular to magnetic field lines in addition to conductivity along the field lines. This produces the Pederson current in the direction \mathbf{E}_\perp of and the Hall current perpendicular to \mathbf{E}_\perp , or along $-\mathbf{E} \times \mathbf{B}$. These currents systems link to the auroral electrojet current system in the ionosphere.

1.5 Magnetospheric Dynamics

The state of the magnetosphere is primarily controlled by the Sun through the solar wind, and the dominant method of momentum coupling is magnetic reconnection, though there is some coupling through momentum transfer usually called viscous interactions of the high speed flow through the magnetopause boundary layer. Geomagnetic activity, such as storms and substorms, occurs when there are perturbations to the Earth's surface magnetic field, which arise from changes in the magnetospheric current systems and ultimately from changes in the solar wind. Almost no geomagnetic activity occurs unless the interplanetary magnetic field is southward which is antiparallel to the Earth's magnetic field on the dayside.

At present, the study of the magnetospheric response through the analysis and prediction of geomagnetic activity is an active effort [2]. This involves determining quantitatively where the solar wind structures are storing the plasma and magnetic energy, how they couple to the magnetosphere, and when this energy is being released into the various parts of the outer and inner magnetosphere, and ionosphere. Because these plasma phenomena are complex and diverse there has been multi-scale modeling of solar-terrestrial processes. To be accurate and useful these

models must be validated with the data. The models range from low order models to MHD simulations that divide the region of interest into small grid cells and the full set of ideal plasma fluid equations is solved in every cell. Global MHD models attempt to study plasma flows and propagation of disturbances as accurately as possible by propagating information between grid points with finite difference equations. These simulations require significant computational resources and provide detailed analysis but are sometimes difficult to interpret. The low order models include the microscopic kinetic theory physics that is critical in boundary layer regions. Boundary regions effect the future in the modeling of the space weather system which will involve an effective hybrid of these modeling types.

1.5.1 Geomagnetic Storms

Prolonged, strong solar wind-magnetosphere coupling will develop a geomagnetic storm of 1-5 days in duration. The *initial phase* of a storm often begins with *sudden storm commencement*, the sudden increase of the surface magnetic field produced by the Chapman-Ferraro magnetopause current (see Section 1.4.2) due to an increase in solar wind dynamic pressure and/or magnetic field. The surface magnetic field then rapidly decreases in the storm *main phase*. This is the delayed response to the strong solar wind-magnetosphere coupling which deposits energy into the magnetotail and strengthens the field aligned currents, and convects particles from the central plasma sheet to the inner magnetosphere. In the first part of the *recovery phase* the surface magnetic field begins to quickly recover (< 12 hours) followed by a longer recovery period (1-2 days). The loss of particles from the radiation belts

leads to a decrease in ring current magnitude, causing the recovery phase of the storm.

1.5.2 Geomagnetic Substorms

Magnetospheric substorms are the most frequent type of geomagnetic activity of which a manifestation is the aurora. The magnetic energy of particles in the magnetotail is abruptly converted to thermal and kinetic energy in a localized region around 1-2 R_E in the central plasma sheet.

The question of substorm onset in the magnetotail is the subject of controversy and there are several theories. Two include: (1) Current disruption/dipolarization at 10 R_E near-Earth magnetotail, (2) Magnetic reconnection farther down tail 20 to 30 R_E . All of these processes occur during substorms however their chronology is unclear. The THEMIS (Time History of Events and Macroscale Interactions during Substorms) mission was designed to address this question by using five identical space probes in Earth orbit and an array of ground based observatories [43][33]. The five spacecraft line up along the magnetotail and measure in situ particle and field data to resolve the physical process of substorm onset and location. First results by Angelopoulos et al. [1] show that tail reconnection is the likely method of substorm initiation, however there is not yet a community consensus.

1.5.3 Geomagnetic Indices

Two geomagnetic activity indices of interest are the AL and the Dst . The AL (auroral lower) index is derived from measurements of the horizontal component of

the Earth's magnetic field at stations located along the auroral oval in the Northern hemisphere [40]. The AL index is compiled every minute over a 24 hour period in a day and is obtained by selecting the most negative values measured among 12 stations located along the auroral zone, all of them above 50° latitude. The most negative values are taken to be the strongest activity of the westward auroral electrojet (from the region 1 field aligned current), which is related to substorm activity. The AU (auroral upper) index is a measure of the dayside eastward auroral electrojet (region 1 field-aligned current) and $AE = AU - AL$ measures the total effect of both electrojets.

The Dst index is a measure of magnetosphere storm activity primarily from the strength of the ring current. The index is obtained from the measurement of the perturbations in the horizontal component of the Earth's magnetic field from ground-based observatories that are sufficiently distant from the auroral and equatorial electrojets and located at approximately $\pm 20^\circ$ latitude, and evenly distributed in longitude [51]. Monthly mean values (neutral-wind-driven conditions), long term changes in the main geomagnetic field, and seasonal variations are subtracted at each station. The Dessler-Parker-Sckopke relation (Equation 1.18) shows that the approximate strength of the ring current contributes to the observed Dst index. Although the ring current has the largest contribution to the Dst all of the magnetospheric current systems have contributions, including the tail current which produces a northward magnetic perturbation at the center of the Earth (decreases Dst), the Chapman-Ferraro magnetopause current which is strengthened during sudden storm commencement and increases the Earth's surface field (sudden positive jump

in Dst), and the magnetopause current system which produces a magnetic perturbation with a direction dependent on the interplanetary magnetic field direction at the bow shock. In laboratory plasma confinement experiments the equivalent of the Dst measure is the diamagnetic loop data which was the earlier sensor used in fusion experiments to measure the total stored plasma energy[12].

Chapter 2

WINDMI Model

2.1 Description

WINDMI is a low dimensional ($d=8$) plasma physics-based model of the coupled magnetosphere ionosphere system [8], [17]. The nonlinear system of eight ordinary differential equations describes the energy transfer between the basic components of the solar WIND driven Magnetosphere-Ionosphere system. The solar wind dynamo voltage (coupling function) is calculated from solar wind parameter data and used to drive the eight equations. The geometry of the model is shown in Figure 2.1 in which the magnetosphere is divided into five regions: (1) the magnetotail lobe with lobe magnetic energy, (2) the central plasma sheet with plasma thermal energy and cross-tail kinetic energy due to plasma flow perpendicular to the field lines, (3) the ring current (4) the nightside region 1 current, and (5) the portion of the nightside region 2 current closing as the partial ring current. The energy associated with regions (3)-(5) is parallel streaming kinetic energy due to plasma flow along field lines. The physical dimensions of the regions are constrained to be time invariant.

The eight dimensional state vector of the system $X = (I, V, p, K_{\parallel}, I_1, V_I, I_2, W_{rc})$ is specified by the equations for the magnetotail lobe with associated current I and voltage V , the mean central plasma sheet with pressure p and parallel kinetic en-

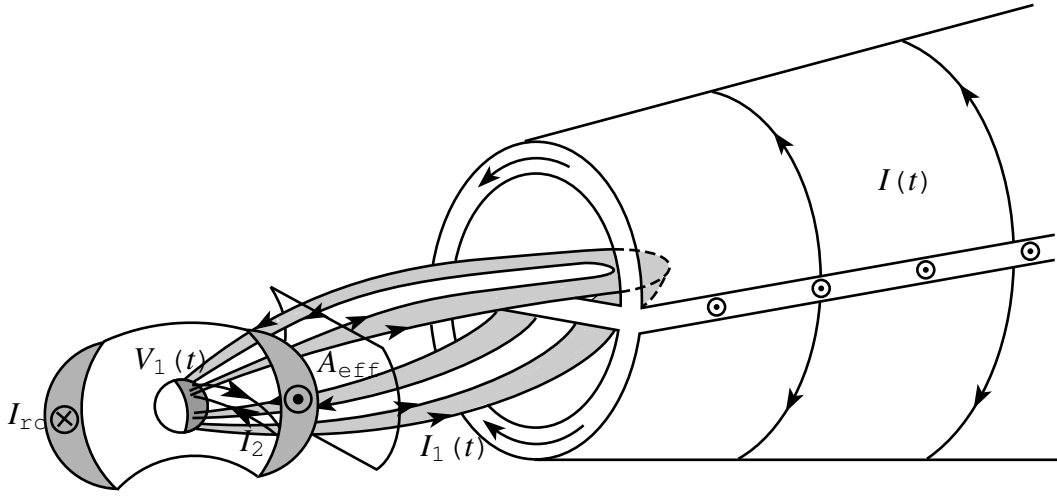


Figure 2.1: WINDMI model geometry of five energy regions (1) the magnetotail lobe with current $I(t)$, (2) central plasma sheet with pressure p and kinetic energy K_{\parallel} (not shown), (3) the ring current I_{rc} with energy W_{rc} and A_{eff} effective aperture for particle injection into the ring current, (4) the nightside region 1 current $I_1(t)$, and (5) the portion of the nightside region 2 current closing as the partial ring current $I_2(t)$.

ergy K_{\parallel} , the ring current with energy W_{rc} , the nightside region 1 current I_1 with voltage V_I , and the portion nightside region 2 current I_2 that closes as the partial ring current.

2.2 WINDMI Development

WINDMI that has grown out of early low-dimensional modeling of the substorms Klimas et al. [24], Klimas et al. [26], Horton and Doxas [15], and Horton and Doxas [16]. Because the magnetosphere is a magnetized conducting fluid, currents are not confined but are free to flow throughout the fluid. These velocity flows and

the magnetic field determine the fluid behavior and produce the resulting currents and electric field. First the procedurally correct application of MHD determines what the currents and electric fields in the magnetosphere are, subsequently these current systems can be modeled in steady state using electrical circuit language[44]. The key plasma currents, voltages, and appropriate plasma volumes are identified and Vlasov partial differential equations are projected on a subspace that contains the relevant dynamical variables for the sub-spatial regions of the total system. The technique has been used in laboratory plasmas to derive ODE systems for the various nonlinear dynamics especially for the edge localized modes called ELMs that have a variety of forms while giving a serious limit on the performance of fusion grade toroidal systems[63].

2.3 WINDMI Differential Equations

The equations for the state vector $X = (I, V, p, K_{||}, I_1, V_I, I_2, W_{rc})$ in the WINDMI model are given by:

$$L \frac{dI}{dt} = V_{\text{sw}}(t) - V + M \frac{dI_1}{dt} \quad (2.1)$$

$$C \frac{dV}{dt} = I - I_1 - I_{\text{ps}} - \Sigma V \quad (2.2)$$

$$\frac{3}{2} \frac{dp}{dt} = \frac{\Sigma V^2}{\Omega_{\text{cps}}} - u_0 p K_{\parallel}^{1/2} \Theta(u) - \frac{pV A_{\text{eff}}}{\Omega_{\text{cps}} B_{\text{tr}} L_y} - \frac{3p}{2\tau_E} \quad (2.3)$$

$$\frac{dK_{\parallel}}{dt} = I_{\text{ps}} V - \frac{K_{\parallel}}{\tau_{\parallel}} \quad (2.4)$$

$$L_I \frac{dI_1}{dt} = V - V_I + M \frac{dI}{dt} \quad (2.5)$$

$$C_I \frac{dV_I}{dt} = I_1 - I_2 - \Sigma_I V_I \quad (2.6)$$

$$L_2 \frac{dI_2}{dt} = V_I - (R_{\text{prc}} + R_{A2}) I_2 \quad (2.7)$$

$$\frac{dW_{\text{rc}}}{dt} = R_{\text{prc}} I_2^2 + \frac{pV A_{\text{eff}}}{B_{\text{tr}} L_y} - \frac{W_{\text{rc}}}{\tau_{\text{rc}}} \quad (2.8)$$

The effective width of the magnetosphere is L_y and magnetotail lobe current I , as discussed in Section 1.4.3, flows in a theta, or two solenoidal, pattern and produces the lobe magnetic energy stored as lobe inductance L . The ring current contains the second largest energy in the magnetosphere system in the form of particle kinetic energy with confinement time τ_{rc} (see Section 1.4.4).

The region 1 field-aligned current (see Section 1.4.5) has a magnetic energy $W_1 = \frac{1}{2} L_1 I_1^2$ and mutual inductance M with the magnetotail cross-field current loop I . Another current loop is the portion of the region 2 field-aligned current which closes on the partial ring current I_2 . Through the partial ring current energy is transferred along the field lines from the ionosphere to the ring current. Another method of energy transfer to the ring current is through particle injection across the Alfvén layer with effective aperture A_{eff} [8].

The high density and pressure central plasma sheet has a thermal energy $U_p = \frac{3}{2}p\Omega_{cps}$ with energy confinement time is τ_E , and pressure gradient driven current $I_{ps} = L_x(p/\mu_0)^{1/2}$. The central plasma sheet volume is $\Omega_{cps} = L_xL_yL_z$ and B_{tr} is the transition region magnetic field. The collisionless microscopic energy transfer processes that occur in the quasi-neutral layer of the central plasma sheet are modeled with a substorm trigger. Fast pressure unloading above a critical current I_c over the interval ΔI can result from current gradient driven tearing modes or cross-field current instabilities as described in [61] and is modeled by the function $\Theta(u) = \frac{1}{2}[1 + \tanh u]$, where $u = (I - I_c)/\Delta I$.

The eight differential Equations 2.1-2.8 are solved numerically to give the eight magnetosphere energy components. The model region 1 field aligned current I_1 flows in the nightside ionosphere E-layer and produces the surface magnetic perturbation ΔB_{AL} from the ambient field which can be compared to AL index data. This is computed using a constant of proportionality $\Delta B_{AL} = -I_1/\lambda_{AL}$ where $\lambda_{AL}=3500$ A/nT when approximating I_1 as a current strip in the E-layer. The model ring current plasma energy W_{rc} is used to compute ΔB_{rc} from the Dessler-Parker-Sckopke relation (Equation 1.18) and compared to Dst index data. In Section 5.7 the addition of new terms in the model Dst are discussed.

2.4 WINDMI Parameters

The WINDMI model has 18 physical parameters which are the coefficients of the differential equations. The parameters relate to the plasma properties and physical dimensions of the system and they can be approximated with physical consid-

erations or from data. The quantities L , C , Σ , L_1 , C_I and Σ_I are the magnetospheric and ionospheric inductances, capacitances, and conductances respectively. A_{eff} is an effective aperture for particle injection into the ring current. The resistances in the partial ring current and region-2 current I_2 regions are R_{prc} and R_{A2} respectively, and L_2 is the inductance of the region-2 current. The coefficient u_0 in Equation 2.3 is a heat flux limiting parameter.

The parameters have been estimated in calculations by Horton and Doxas [15], Horton and Doxas [16], and Doxas et al. [8]. and these nominal parameter values are shown in Tables 2.1 and 2.2. [48] have allowed the parameters to vary over physically allowable ranges to optimize the WINDMI AL and Dst prediction by implementing a genetic algorithm.

2.5 WINDMI Input

2.5.1 Solar Wind Data from ACE

The ACE spacecraft has a halo orbit about the L1 Lagrange point located approximately 1.5×10^6 km or $235 R_E$ from the Earth[50]. The solar wind proton density n_{sw} and solar wind velocity $\mathbf{v}_{sw} = (v_x^{sw}, v_y^{sw}, v_z^{sw})$ are available at a 64 second resolution. The interplanetary magnetic field $\mathbf{B}_{IMF} = (B_x^{IMF}, B_y^{IMF}, B_z^{IMF})$ are given at a cadence of 16 seconds. Missing data points are replaced with the previously available points, and all of the data are linearly interpolated to the time stamp needed by the integration time step.

The data is time delayed from the ACE spacecraft position to the approximate magnetopause (MP) standoff distance, where coupling to the magnetopause

Table 2.1: WINDMI Nominal Parameters, estimated by physical considerations of the state and geometry of the nightside magnetosphere using the Tsyganenko magnetic field model[55].

Parameter	Value	Description
L	90 H	Inductance of the lobe cavity surrounded by the magnetotail current $I(t)$.
M	1 H	The mutual inductance between the nightside region 1 current loop I_1 and the magnetotail current loop I .
C	50000 F	Capacitance of the central plasma sheet in Farads.
Σ	8 S	Large gyroradius ρ_i plasma sheet conductance from the quasineutral layer of height $(L_z \rho_i)^{1/2}$ about the equatorial sheet.
Ω_{cps}	$2.6 \times 10^{24} \text{ m}^3$	Volume of the central plasma sheet that supports mean pressure $p(t)$, initial estimate is $10^4 R_E^3$.
u_0	$4 \times 10^{-9} \text{ m}^{-1} \text{ kg}^{-1/2}$	Heat flux limit parameter for parallel thermal flux on open magnetic field lines $q_{\parallel} = const \times v_{\parallel} p = u_0 (K_{\parallel})^{1/2} p$. The mean parallel flow velocity is $(K_{\parallel} / (\rho_m \Omega_{cps}))^{1/2}$.
I_c	$1.78 \times 10^7 \text{ A}$	The critical current above which unloading occurs.
α	8×10^{11}	The magnetotail current driven by the plasma pressure p confined in the central plasma sheet. Pressure balance between the lobe and the central plasma sheet gives $B_{\ell}^2 / 2\mu_0 = p$ with $2L_x B_{\ell} = \mu_0 I_{ps}$. This defines the coefficient α in $I_{ps} = \alpha p^{1/2}$ to be approximately $\alpha = 2.8 L_x / \mu_0^{1/2}$.

Table 2.2: WINDMI Nominal Parameters, estimated by physical considerations of the state and geometry of the nightside magnetosphere using the Tsyganenko magnetic field model.

Parameter	Value	Description
τ_{\parallel}	10 min	Confinement time for the parallel flow kinetic energy K_{\parallel} in the central plasma sheet.
τ_E	30 min	Characteristic time of thermal energy loss through earthward and tailward boundary of plasma sheet.
L_1	20 H	The self-inductance of the wedge current or the night-side region 1 current loop $I_1(t)$
C_I	800 F	The capacitance of the nightside region 1 plasma current loop.
Σ_I	3 mho	The ionospheric Pedersen conductance of the westward electrojet current closing the I_1 current loop in the auroral (altitude ~ 100 km, 68°) zone ionosphere.
R_{prc}	0.1 ohm	The resistance of the partial ring current.
τ_{rc}	12 hrs	The decay time for the ring current energy.
L_2	8 H	The inductance of the region 2 current.
R_{A2}	0.3 ohm	Resistance of the region 2 footprint in the Auroral Region.
B_{tr}	5×10^{-9} T	The magnetic field in the transition region.
A_{eff}	$8.14 \times 10^{13} m^2$	The average effective area presented to the magnetotail plasma for plasma entry into the inner magnetosphere, estimated to be $2R_E^2$.
L_y	3.2×10^7 m	The effective width of the Alfvén layer aperture, estimated to be $5R_E$.
ΔI	1.25×10^5 A	The rate of turn-on of the unloading function.

occurs. The time delay t_{delay} is approximately one hour and is computed using the formula

$$t_{\text{delay}} = \frac{X_{\text{ACE}} - \bar{X}_{\text{MP}}}{\bar{v}_{\text{sw}}} \quad (2.9)$$

The average x coordinate of the ACE spacecraft in GSM coordinates is X_{ACE} . The magnetopause standoff distance X_{MP} is taken as $10 R_{\text{E}}$ for WINDMI runs and for real-time WINDMI it is taken as the average magnetopause standoff distance over the storm period calculated from the Shue et al. [42] formula. The velocity \bar{v}_{sw} is taken to be the average x velocity during the event, or the average bulk velocity for real-time runs. The more accurate time delay formulas of Weimer et al. [59], Bargatze et al. [4] which apply the minimum variance analysis to the IMF time series are being implemented for future studies. Solar wind propagation delay of in-situ spacecraft measurements in a handful of locations in the vast inner heliosphere remains an important unresolved problem. The propagated solar wind parameters are then used to derive a series of input solar wind driving voltages for the WINDMI model.

2.5.2 Solar Wind-Magnetosphere Coupling Functions

Solar wind dynamo voltage is generated in the Earth’s frame from conducting plasma with frozen in magnetic field moving past it. $\mathbf{E} = -\mathbf{u}_{\text{sw}} \times \mathbf{B}$. The term “dynamo” is borrowed from electrical engineering to describe the energy flow associated with magnetic reconnection at the magnetopause. There are several candidate coupling functions for the driving voltage and three are considered in this work: the

Rectified, Siscoe, and Newell coupling functions.

The Rectified driving voltage [5, 39] is given by $v_{\text{bulk}} B_{\text{S}}^{\text{IMF}} L_y^{\text{eff}}$, where v_{bulk} is solar wind bulk velocity in GSM coordinates, $B_{\text{S}}^{\text{IMF}}$ is the southward IMF component ($B_{\text{S}}^{\text{IMF}} = -B_z^{\text{IMF}}$ for $B_z^{\text{IMF}} < 0$) and $L_y^{\text{eff}} \approx 10R_{\text{E}}$ is an effective cross-tail width over which the dynamo voltage is produced. The half-wave rectified dynamo voltage has a base voltage of 40 kV for northward IMF $B_z^{\text{IMF}} \geq 0$ and for southward IMF $B_z^{\text{IMF}} < 0$ the driving voltage is

$$V_{\text{sw}}^{\text{Bs}} = 40(\text{kV}) + v_{\text{bulk}} B_{\text{S}}^{\text{IMF}} L_y^{\text{eff}} \quad (2.10)$$

The second coupling function is given by [45], [46], and [35] as the potential drop around the magnetopause from magnetic reconnection in the absence of saturation mechanisms. The formula is given by

$$V_{\text{sw}}^{\text{S}} (\text{kV}) = 30.0(\text{kV}) + 57.6 E_{\text{sw}} (\text{mV/m}) P_{\text{sw}}^{-1/6} (\text{nPa}) \quad (2.11)$$

where $E_{\text{sw}} = v_{\text{bulk}} B_{\text{T}} \sin(\frac{\theta}{2})$ is the solar wind electric field with respect to the magnetosphere and the dynamic solar wind pressure $P_{\text{sw}} = n_{\text{sw}} m_{\text{p}} v_{\text{bulk}}^2$. The perpendicular component of the the magnetic field is given by $B_{\text{T}} = (B_y^2 + B_z^2)^{1/2}$. Here m_{p} is the mass of a proton and only the proton density contribution has been included in n_{sw} . The IMF clock angle θ is given by $\tan^{-1}(B_y/B_z)$.

Newell et al. [34] compared the correlation of 20 candidate coupling functions with geomagnetic indices. The function which represents the rate of magnetic flux

$d\Phi_{\text{MP}}/dt$ opening at the magnetopause correlated best with 9 out of 10 indices and it is our third coupling function, given as

$$d\Phi_{\text{MP}}/dt = v_{\text{bulk}}^{4/3} B_{\text{T}}^{2/3} \sin^{8/3}\left(\frac{\theta}{2}\right). \quad (2.12)$$

The driving voltage can be calculated as

$$V_{sw}^{\text{N}} = 40(\text{kV}) + \nu d\Phi_{\text{MP}}/dt, \quad (2.13)$$

hereinafter referred to as the Newell driving function. The unit conversion factor $\nu = \overline{V_{sw}^{\text{Bs}}}/\overline{d\Phi_{\text{MP}}/dt}$ has been added for correct WINDMI model input units and it is the ratio of the average Rectified voltage to the magnetic flux for the storm period. In the Newell et al. [34] study only correlations were computed and therefore specific units were not necessary.

Chapter 3

Effect of Interplanetary Shocks on the AL and Dst Indices

3.1 Introduction and Methodology

In order to understand the effect of IP shock/sheath events on geomagnetic activity, the WINDMI model is used. Analytic solar wind plasma fields are constructed from ACE data for the 3-6 October 2000 event and derive an analytic input driving voltage. Solar wind velocity and magnetic field strength variation across interplanetary shocks are correlated with the Dst index [11]. In addition multiple interplanetary magnetic structures are more geoeffective than single interplanetary magnetic structures [10]. Shock effects on the aurora as measured by the FAST and DMSP satellites have been studied by Zhou et al. [62]. It was found that there was a significant increase in electron precipitation the dawnside and duskside auroral oval zone after the shock/pressure pulse arrivals. There are three basic phenomena that can lead to perturbations in the AL and Dst : 1) the CME, as defined by its composition or magnetic field configuration 2) the sheath compressed solar wind and 3) the shock itself. The role of the shock events are examined by removing both the shock and sheath features individually from each analytic plasma field: solar wind density, velocity, and interplanetary magnetic field (IMF) magnitude, then examining the change in the WINDMI output of AL and Dst . Analysis of the WINDMI AL and

Dst results for these events using ACE data as input is given in Spencer et al. [48].

3.2 Analytic ACE Data

The analytic fits to the ACE data were constructed using hyperbolic tangent functions. To study the role of the shock, the shock and sheath features are removed from the solar wind parameters (u_{sw} , n_{sw} , B_{\perp}) individually while the ICME signature is kept. The shock and sheath features were removed from the data for the duration of the shock time up until before the associated ICME signatures. The methodology is to test the effect of each shock/sheath feature on the geospace response by removing the feature from the analytic fields while the other fields downstream remain unchanged.

To compute an analytic driving voltage, fields for solar wind velocity u_{sw} , proton density n_{sw} , and magnetic field magnitude B_{\perp} were created. Figure 3.1 shows how the model fields without the compressional jumps in the solar wind $B_{\perp} = (B_y^2 + B_z^2)^{1/2}$ are expressed for the April 2002 storm. The three curves in the top panel give the analytic model B_{\perp} profile with the first S1 (dashed line), second S2 (dotted line), and third S3 (solid line) shock/sheath features individually removed. The bottom panel shows the ACE magnetometer data for the B_{\perp} signal.

It is recognized that the self-consistent steady state shock models would require that the jump in B_{\perp} and the density be kept or dropped simultaneously. In practice the shocks are not satisfying the steady state constraints and so the

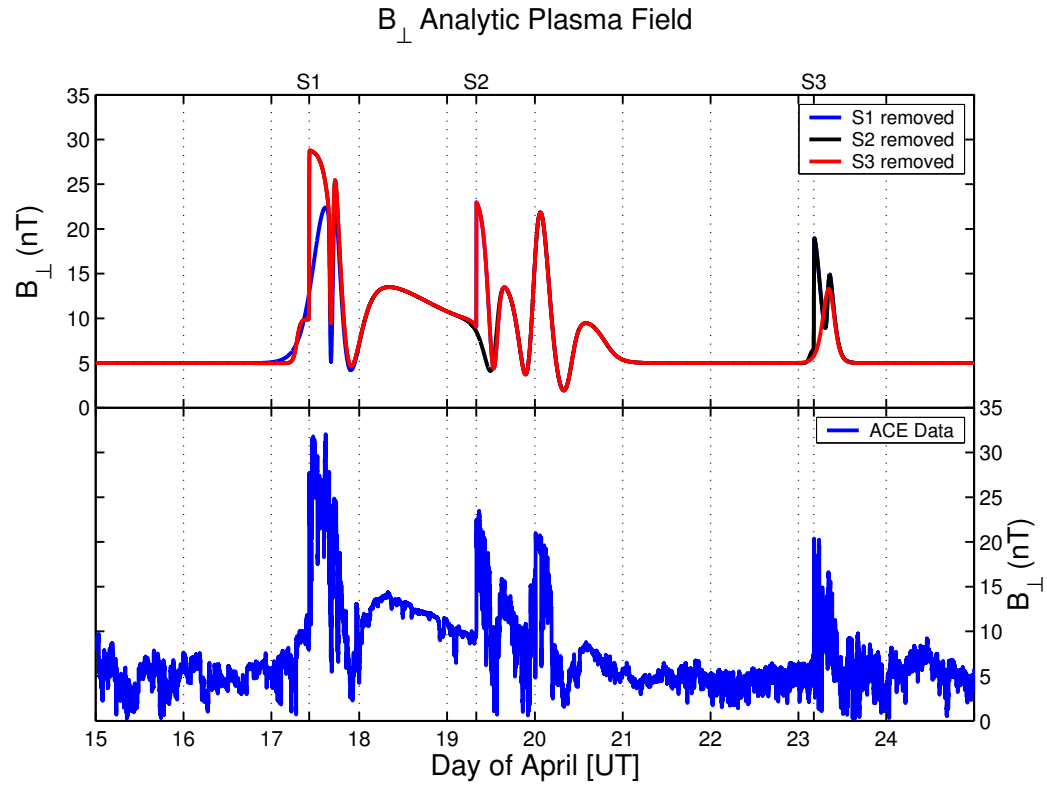


Figure 3.1: The bottom panel shows the ACE data for the solar wind $B_{\perp} = (B_y^2 + B_z^2)^{1/2}$ during the April 2002 storm. The top panel shows the analytic parameter for the solar wind B_{\perp} for which certain shock/sheath features have been removed from the analytic shock field based on the ACE data.

structures appear with a variety of jumps. From another perspective, the use of independent jumps in the magnetic and density fields can be viewed as virtual displacements as used in classical mechanics.

Figure 3.1 bottom panel shows the ACE data for the solar wind $B_{\perp} = (B_y^2 + B_z^2)^{1/2}$ during the April 2002 storm. The top panel shows the analytic plasma field for the solar wind B_{\perp} for which certain shock features have been removed from the analytic shock field based on the ACE data.

The solar wind driving voltage was calculated using the Siscoe Eq. 2.11 described in subsection 2.5.2 with the analytic solar wind fields with and without the shock/sheath feature. Using this input solar wind driving voltage the model outputs were compared with and without the shock/sheath.

3.3 Event Descriptions and WINDMI Analysis

3.3.1 15-24 April 2002

In Figure 3.2 ACE data during this period shows three fast forward shock events which signal the arrival at Earth of CMEs from solar eruptions on 15, 17, and 21 April. ACE IMF data and compositional signatures (elevated oxygen charge states O^{7+}/O^{6+} and unusually high Fe charge states) were used to identify the signatures of the ICME in the data. The first shock event (S1) was observed by ACE at 1020 UT on 17 April moving at the calculated shock speed of 480 km/s and is associated with a halo CME with brightness asymmetry observed by SOHO/LASCO at 0350 UT on 15 April moving at the plane-of-sky speed of 720 km/s away from the Sun [31]. The CME driving the shock is observed by ACE as a MC beginning at

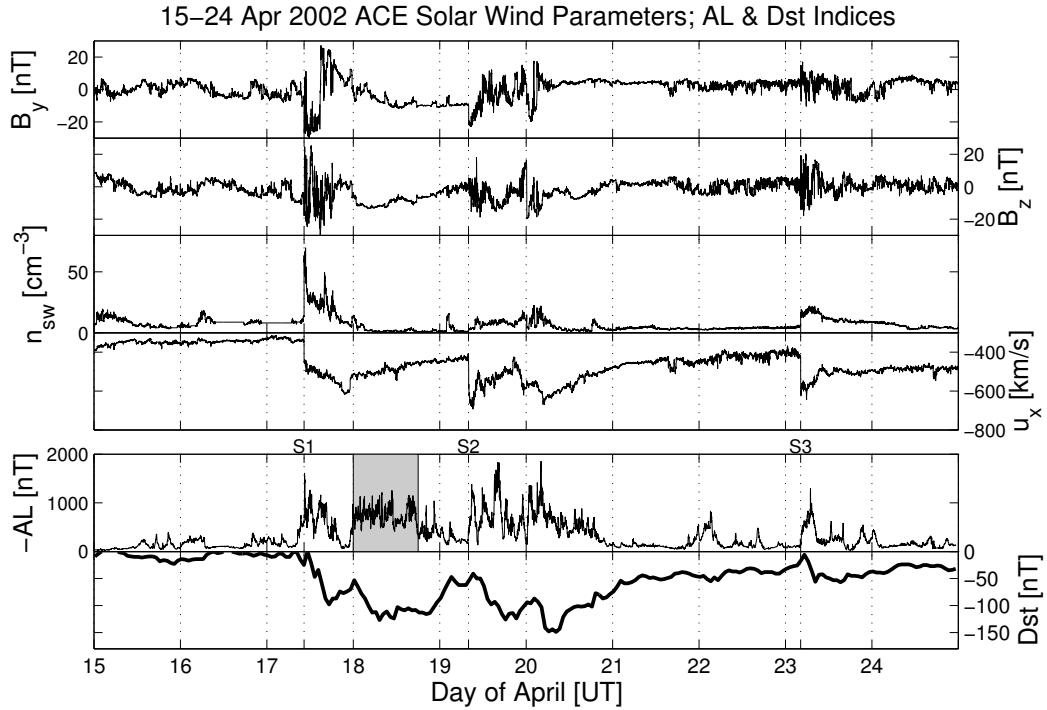


Figure 3.2: Top panels: ACE solar wind data for 15-24 April 2002 in GSM coordinates showing the interplanetary magnetic field components B_y and B_z , proton number density n_{sw} , and solar wind flow velocity $u_x(t)$. Three interplanetary shocks are identified by S1, S2, S3 occurring at 1020 UT 17 April, 0801 UT 19 April, and 0414 UT 23 April. Bottom panels: The corresponding time advanced AL and Dst data during this period shows substorm (shaded) and storm activity.

the start of 18 April and continuing until approximately 1900 UT. The shock and sheath features in the data are taken from 1020 UT (S1) to 1450 UT on 17 April. Seven sawtooth oscillations were observed on 18 April from about 0200 UT to 2100 UT whose signature can be seen in the AL shown in the bottom panels of Figure 3.2 as the shaded region. The Dst , also shown in this figure, reaches a -127 nT during this time.

The second shock event (S2) was observed at 0801 UT on 19 April with a speed of 650 km/s and is associated with a halo CME with outline asymmetry which left the Sun at 0826 on 17 April moving with the plane-of-sky speed of 1240 km/s [6]. The shock on April 19 was followed by a more complicated solar wind disturbance observed by ACE from 1500-2000 UT 19 April and 1000 UT 20 April to 1200 UT 21 April likely resulting from a subsequent CME which dynamically interacts with the perturbation ahead. The interacting signatures looked qualitatively comparable to the well-documented case of October-November 2003 [65], but with clear signatures of solar wind between the two interacting CMEs. The shock/sheath features are taken from 0801 UT (S2) to 1300 UT on 19 April. This solar wind disturbance triggered a magnetic storm with *Dst* minima of -126 nT and -124 nT building up in the main phase and -148 nT and -149 nT at storm peak. The third shock event (S3) arrived during the recovery phase at 0413 UT on 23 April with a speed of 680 km/s and is associated with an X-class flare and partial halo CME with outline asymmetry leaving the Sun at 0127 UT on 21 April with the plane-of-sky speed of 2393 km/s. The magnetosphere was clipped by the shock/sheath region rather than the ICME, producing a weak magnetic storm with minimum *Dst* of only -56 nT. Halo CMEs experience maximum projection effects in coronagraph images and therefore the plane-of-sky speeds should be taken as a lower limit of the actual speed. The shock dates and times are listed in Table 3.1 and the date, time and speed of the associated CMEs are taken from the SOHO LASCO CME catalog [60].

Table 3.1: A listing of observed ACE IP Shock dates, times, and calculated speeds (assuming a parallel shock) during 15-24 April 2002, with associated SOHO CME times and speeds. Dates of observed magnetic cloud structure in ACE IMF B_y , B_z , and clock angle are also listed.

Shock (UT)	Speed (km/s)	ICME Signature	CME (UT)	Speed (km/s)
17 Apr 1020	480	1800 UT 17 Apr-1900 UT 18 Apr	15 Apr 0350	720
19 Apr 0801	650	1500-2000 UT 19 Apr 1000 UT 20 Ap-1200 UT 21 Apr	17 Apr 0826	1240
23 Apr 0414	680	none	21 Apr 0127	2393

In Figure 3.3 the WINDMI results from runs using both data and analytic input fields are compared to results from which the shock/sheath feature has been removed from B_{\perp} . The analytic shock field B_{\perp} without all three δB_{\perp} shock/sheath features (top panel of Figure 3.1), and ACE data for the u_{sw} and n_{sw} parameters were used to derive the input solar wind dynamo voltage shown in the top panel of Figure 3.3 (solid black line). WINDMI $-AL$ and Dst results for this input are shown in the middle and bottom panels (dashed lines), respectively. When the δB_{\perp} shock/sheath feature is removed there is a significant decrease of 50% in the AL peaks -1600 nT (17 April 1100 UT), -1824 nT and -1851 nT (19 April 1648 UT and 20 April 0451 UT), and -1297 nT (23 April 0741 UT) associated with these shocks. Model results for the Dst (bottom panel of Figure 3.3) show a $-Dst$ decrease of 10-20% for roughly 12 hours after the first shock (17 April 1120 UT to 18 April 0700 UT) and a decrease of 20%-30% after the second shock (19 April 0900 UT to 20 April 0400 UT).

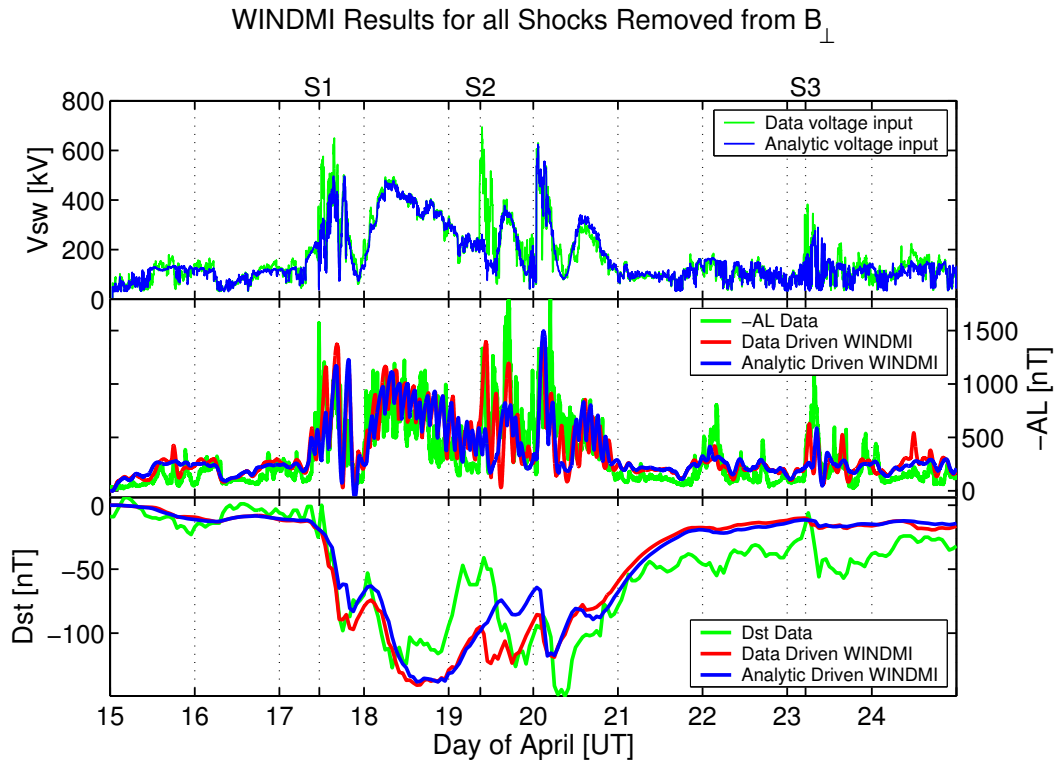


Figure 3.3: WINDMI results for V_{sw} input derived from solar wind parameter data or analytic parameters for which all three shock/sheath features have been removed from B_{\perp} . The analytic shock field B_{\perp} without the shock/sheath features (top panel of Figure 3.1), and ACE data for the u_{sw} and n_{sw} parameters was used to derive the input solar wind dynamo voltage shown in the top panel. WINDMI $-AL$ and Dst results for this input are shown in the middle and bottom panels (dashed lines), respectively. decrease of 50% in the three AL peaks times and there is

The jump δB_{\perp} has the most significant impact on the AL and Dst compared to the other parameters. Removing the shock/sheath features from u_{sw} produces a slight decrease of 15%, 25% and 10% in the first, second, and third AL peaks respectively. There is only a slight increase of 10% and 5% of the first and third AL peaks when the shock/sheath features are removed from n_{sw} . The compressional jump δn_{sw} is only $\sim 2cm^{-3}$ for the second shock event. When the shock/sheath features are removed from all of the plasma fields (B_{\perp}^{IMF} , u_{sw} , n_{sw}) the $-AL$ peaks decrease by a similar amount as when the δB_{\perp} features are removed only. The jump δB_{\perp} has the most impact on producing the three $-AL$ peaks during this storm. The second shock/sheath combination on 19 April at 0801 UT which produced AL peaks of -1824 nT and -1851 nT is the most effective of the three shocks.

3.3.2 3-6 October 2000

An unusual feature of the 3-6 October 2000 solar wind driver was the appearance of a fast forward shock advancing into a preceding magnetic cloud [57]. ACE data shows a magnetic cloud from 3 October at 1018 UT through 5 October at 0534 UT lasting about 42 hours. The signature of the magnetic cloud can be seen from the sinusoid-like waveforms of B_y^{IMF} and B_z^{IMF} as the IMF clock angle changes linearly through an angle of 180° during this period. The fast forward shock occurs at 0240 UT on 5 October with a calculated shock speed of 534 km/s and compression ratio of 2.3. There are jumps in the velocity from 364 km/s to 460 km/s, in the proton density from $7cm^{-3}$ to $16cm^{-3}$, and in perpendicular magnetic field from 7 nT to 16 nT across the shock front.

The AL data shows a first large spike with a peak of -1938 nT occurring at 0651 UT on 5 October 2000. A second, larger spike of approximately -2790 nT in the AL index occurs at 1210 UT on 5 October 2000 initiated by a strong southward IMF excursion detected at ACE about an hour earlier. Periodic substorms occur in the interval of 0600-1200 UT 4 October and have been identified as sawtooth oscillations by Huang et al. [18] and Reeves et al. [38]. The Dst minimum of -180 nT is reached on 5 October slightly after the strong southward IMF surge. Consistent with April 2002 analysis, when the shock/sheath feature is removed from B_{\perp} the first AL peak of -1938 nT occurring at 0720 UT 5 October 2000 decreased by $\sim 50\%$. There is also a decrease of $-Dst$ by $\sim 25\%$ after the shock arrival time. The AL peak only decreases by 10% when the shock/sheath is removed from u_{sw} and the removal of the feature from n_{sw} produces an increase of 10% in the AL peak. Again, when the shock is dropped from all three plasma fields the result is similar to removing the δB_{\perp} shock only. These results demonstrate that the first large AL peak was triggered by the shock/sheath front, and most strongly by the δB_{\perp} jump.

3.4 Conclusions

The question of how much IP shock/sheath events contribute to the geo-effectiveness of solar wind drivers was examined based on a series of numerical experiments with WINDMI using observed solar wind drivers for the 15-24 April 2002 and 3-6 October 2000 events, each of which had interesting shock features. In these experiments, analytic fits to solar wind input parameters (B_{\perp}^{IMF} , u_{sw} , and n_{sw}) allowed shock/sheath features to be easily removed while leaving other features

of the solar wind driver undisturbed. Percent changes in WINDMI-derived AL and Dst indices between runs with and without the observed shock/sheath feature were taken as a measure of its relative contribution to the geoeffectiveness. The interplanetary shock/sheath events during these storm periods are strongly related to storm and substorm geomagnetic activity predicted by the WINDMI model.

The δB_{\perp} jumps at the shocks/sheath have a strong impact on the three AL peaks during the April 2002 storm. During the October 2000 storm the first large AL spike was triggered by the shock/sheath feature in B_{\perp} . The *Siscoe et al.* solar wind dynamo voltage includes contributions from the number density, clock angle, and B_y^{IMF} ($B_{\perp}^{IMF} = (B_y^2 + B_z^2)^{1/2}$) which are not included in the rectified $u_{sw}B_zL_y$ dynamo voltage more typically used. This is particularly important for the April 2002 shocks in which, for example, the second shock had a $\delta B_z^{IMF} < 1$ nT while $\delta B_y^{IMF} \sim 10$ nT therefore producing dynamo voltage $V_{sw}=600$ kV while the rectified voltage is only 200 kV.

The solar wind-magnetosphere coupling dynamics is most sensitive to variations in the solar wind velocity and interplanetary magnetic field. This can be seen from the equation for the input Siscoe solar wind dynamo voltage where the input $V_{sw} \propto u_{sw}^{2/3} n_{sw}^{-1/6} B_{\perp}^{1/2}$ so it is expected that the removal of the shock compressional feature in the velocity and magnetic field parameters to decrease the driving voltage V_{sw} , and in the number density to increase V_{sw} . During these storms the magnetic field components have a 1.5-3 times increase across the shock front while the velocity does not increase by more than 1.5 times. The jump in the number density can be as high as 4 times the upstream value, however, the $n_{sw}^{-1/6}$ dependence in

the calculated V_{sw} hides this effect. Also shock features in the velocity and number density increase the solar wind dynamic pressure which causes the magnetopause to move close to the Earth and produces stronger coupling.

Chapter 4

Real-Time WINDMI Model

4.1 Introduction

The rapid forecasting of magnetospheric storms and substorms from solar wind data with reliable models is of wide interest and important for protecting the space infrastructure of communication and global positioning spacecrafts. There are basic constraints from plasma physics that forecasting models must observe. The models need to forecast the standard geomagnetic indices used to define substorms and storms such as the AL and Dst indices.

Real-Time WINDMI, an extension of WINDMI, is used to predict AL and Dst values approximately one hour before geomagnetic substorm and storms event. Subsequently, every ten minutes ground based measurements compiled by WDC Kyoto are compared with model predictions (<http://orion.ph.utexas.edu/~windmi/realtime/>). The performance of the Real-Time WINDMI model is quantitatively evaluated for twenty-two storm/substorm event predictions from February 2006 to August 2008. Three possible input solar wind-magnetosphere coupling functions are considered (Section 2.5.2): the standard Rectified coupling function, a function due to Siscoe, and a recent function due to Newell. Model AL and Dst predictions are validated using the average relative variance (ARV), correlation coefficient (COR), and root mean squared error (RMSE).

There are many models for the *Dst*, including Burton et al. [5], Klimas et al. [25], O’Brien and McPherron [36], Temerin and Li [52, 53]. Models for the electrojet currents and the *AL* index include Bargatze et al. [3], Klimas et al. [26], Klimas et al. [24], Li et al. [28]. Temerin and Li [53] have reported a high accuracy in *Dst* prediction with COR=0.956, PE=0.914, and RMSE=6.65 nT for the period of 1995-2002. The complex empirical *AL* model of Li et al. [28] achieves COR=0.795, PE=0.524, and RMSE=88 nT for 1997-2001. The comparison of Real-Time WINDMI with other *AL* and *Dst* models is being considered for analysis as model results during solar maximum are accumulated.

4.2 Real-Time WINDMI

For Real-Time WINDMI nominal values of the WINDMI parameters are used for all events. The parameters can also be optimized (against the Quicklook *Dst* data) within physically allowable ranges, using a genetic algorithm. The optimized results are only meaningful when the real-time Quicklook *Dst* data is available and reliable.

The three coupling functions described in Section 2.5.2 are calculated similarly to WINDMI, except real-time ACE solar wind data is used. Real-time measurements of solar wind proton density n_{sw} , solar wind bulk velocity v_{bulk} , and interplanetary magnetic field B_{IMF} are available from ACE in one minute intervals.

Every ten minutes the data and WINDMI model predictions for the concurrent runs are shown on the website: <http://orion.ph.utexas.edu/~windmi/realtime/>. WINDMI model runs can also be requested from the Community Coordinated Mod-

eling Center (<http://ccmc.gsfc.nasa.gov/>). For this work the trigger threshold for storm activity is set to a *Dst* level of below -50 nT and for substorm activity the trigger threshold is set to an *AL* level of below -500 nT. There is an automated email alert system which notifies of predicted activity.

4.3 Measures of Performance

For a time series $i = 1, 2, \dots, N$ of predicted model values x_i and observed data values y_i , three measures of the agreement between the model and the data are used.

The average relative variance (ARV) is the primary measure used and is given by

$$ARV = \frac{\sum_i (x_i - y_i)^2}{\sum_i (\bar{y} - y_i)^2} \quad (4.1)$$

The ARV approaches zero when the model output and data converge to each other. When the ARV is equal to one then the model is only as good as the average of the data. The prediction efficiency (PE) is given by $PE = 1 - ARV$.

The correlation coefficient (COR) is given by

$$COR = \frac{\sum_i (x_i - \bar{x})(y_i - \bar{y})}{\sigma_x \sigma_y} \quad (4.2)$$

and is a measure of how well correlated the model is to the data with $COR = 0$ meaning they are uncorrelated, $COR > 0$ for a positive correlation, and $COR < 0$ for a negative correlation.

The root mean squared error (RMSE) quantifies the amount by which the model differs from the data and is given by

$$RMSE = \sqrt{\sum_i (x_i - y_i)^2 / N} \quad (4.3)$$

The RMSE has the units of the data (nT) and thus is useful for inferring the range of uncertainty in the predicted signal. Small RMSE values are indications of model results in good agreement with data.

4.4 Real-Time WINDMI Results: February 2006 - August 2008

4.4.1 Event Selection

Twenty-two storms and or substorm events between February 2006 - August 2008 were selected for model performance analysis. The events are shown in Table 4.1 and were selected based on Real-Time WINDMI results triggering on a threshold of $Dst \leq -50$ nT or $AL \leq -400$ nT. This is only a subset of larger substorm events between February 2006 - August 2008 that meet this criteria and there were many other mostly smaller substorm events during this period that are not well defined. The time interval was selected such that the initial, main, and recovery phases of the Dst signature were included. The time interval must also include any AL activity above 400 nT but starts and ends with a “quiet-time” AL of less than 100-200 nT.

The WDC Kyoto minimum Dst and AL data and Real-Time WINDMI minimum Dst and AL predictions for both input drivers are also shown in Table 4.1. Seven of the twenty-two events had sudden storm commencement. The mean Dst index data is -64.3 nT and and the mean AL index is -1252.6 nT for these

selected events. The time interval chosen for each event was determined using both *AL* and *Dst* data. The time interval used to evaluate model performance was a subset of each event only during a shorter period around which storm or substorm activity was above the threshold. For each event, the given activity time range was fixed for both *AL* and *Dst* comparisons.

4.4.2 Model Performance

Concurrent runs of the Real-Time WINDMI model are performed using the input solar wind Rectified driver, Siscoe driver, or Newell driver with WINDMI model nominal parameters. The model parameters are held fixed for all driver inputs and events and therefore variations in the model output are due to differences in the driving voltage. The performance of the model was measured with the average relative variance (ARV), correlation coefficient (COR), and root mean squared error (RMSE) for each event. These metrics are defined in Section 4.3. In this work ACE Level 2 data was used in the calculations instead of ACE real-time data which is normally used on the Real-time WINDMI website. WDC Kyoto *AL* and *Dst* data and model comparisons were calculated using provisional values when available. For this work, provisional *AL* data was available for all of the events, *Dst* data was provisional up to January 2007, and so Quicklook *Dst* data was used for the remaining events.

The mean *AL* and *Dst* ARV of all of the events is shown in Table 4.2 for the three input coupling functions. In Table 4.3 the mean *AL* and *Dst* correlation coefficient is shown. For the twenty-two events, the *AL* prediction performance has

Table 4.1: The list of 22 events for which storms and/or substorms have been predicted by Real-Time WINDMI from February 2006 to August 2008. The WDC Kyoto minimum *Dst* and *AL* data for each event are given in the first two columns.

Date	Data ^a		Real-Time WINDMI ^b	
	Min. Dst (nT)	Min. AL (nT)	Dst (nT)	Min. AL (nT)
2-8 Apr 2006 ^c	-87	-1179	-26/-40/-45	-270/-341/-267
8-11 Apr 2006	-80	-1045	-40/-35/-47	-402/-395/-461
13-18 Apr 2006	-111	-1598	-125/-134/-122	-1123/-1000/-1017
6-9 Aug 2006	-44	-1556	-31/-42/-46	-398/-406/-465
17-23 Aug 2006	-71	-1697	-68/-56/-87	-758/-426/-811
23-26 Sep 2006 ^c	-56	-1167	-20/-27/-30	-347/-307/-380
20-22 Oct 2006 ^c	-28	-822	-17/-33/-27	-224/-348/-320
9-12 Nov 2006	-51	-1622	-37/-43/-45	-709/-436/-460
29 Nov to 1 Dec 2006	-74	-1704	-49/-47/-63	-432/-370/-451
5-8 Dec 2006 ^c	-48	-1175	-28/-34/-40	-386/-318/-379
14-18 Dec 2006	-146	-2349	-180/-193/-228	-1779/-1423/-1752
28-31 Jan 2007	-40	-1296	-30/-38/-38	-533/-428/-506
22-27 Mar 2007	-69	-1032	-43/-36/-66	-400/-348/-602
31 Mar to 4 Apr 2007	-63	-813	-27/-26/-37	-380/-332/-401
16-19 Apr 2007 ^c	-47	-584	-22/-38/-37	-311/-381/-385
27 Apr to 1 May 2007	-56	-942	-29/-32/-43	-399/-349/-454
21-26 May 2007	-63	-1259	-54/-48/-61	-736/-437/-699
10-13 Jul 2007	-40	-896	-27/-35/-58	-375/-350/-814
13-17 Jul 2007	-46	-891	-38/-33/-63	-410/-342/-746
25-28 Oct 2007	-51	-1047	-25/-32/-37	-364/-381/-436
19-23 Nov 2007	-71	-1552	-41/-82/-57	-654/-855/-716
7-10 Mar 2008	-72	-1332	-39/-37/-50	-937/-440/-856

^aThe *AL* data are provisional, the *Dst* data are provisional up to January 2007, and from January 2007 onwards the *Dst* data are Quicklook. The minimum Real-Time WINDMI *Dst* and *AL* predictions are given for the Rectified, Siscoe, and Newell input drivers in the last two columns.

^bHere the first value is the result using Rectified input driver V_{sw}^{Bs} (Equation 2.10), the second value is the result using the Siscoe input driver V_{sw}^S (Equation 2.11), and the third value is the result using the Newell input driver V_{sw}^N (Equation 2.13).

^cThe model *AL* and *Dst* did not reach the defined activity threshold for the alerts and were not detected. They are close to the thresholds and are included here for statistical analysis.

Table 4.2: Mean Average Relative Variance (ARV) measures of Real-Time WINDMI model results with the *AL* and *Dst* index are shown in the second and third columns. for the selected events from February 2006 - August 2008 (listed in Table 4.1). The ARV is calculated using Equation 4.1 in Section 4.3.

Feb. 2006 - Aug. 2008 Selected Events, Mean ARV		
Input	Mean <i>AL</i> ARV	Mean <i>Dst</i> ARV
<i>Rectified</i> V_{sw}^{Bs}	0.38 ± 0.21	0.37 ± 0.27
<i>Siscoe</i> V_{sw}^S	0.41 ± 0.16	0.42 ± 0.23
<i>Newell</i> V_{sw}^N	0.33 ± 0.17	0.54 ± 0.39

Table 4.3: Mean correlation coefficient (COR) of Real-Time WINDMI model results with the *AL* index are shown in the second column and with the *Dst* index in the fourth column. The third column shows the mean direct correlation between the calculated input driving voltage V_{sw} and the *AL* index. The COR is calculated using Equation 4.2 in Section 4.3.

Feb. 2006 - Aug. 2008 Selected Events, Mean COR			
Input	Mean <i>AL</i> COR	Mean <i>AL</i> Direct COR	Mean <i>Dst</i> COR
<i>Rectified</i> V_{sw}^{Bs}	0.62 ± 0.13	0.40 ± 0.20	0.80 ± 0.12
<i>Siscoe</i> V_{sw}^S	0.52 ± 0.15	0.37 ± 0.18	0.77 ± 0.13
<i>Newell</i> V_{sw}^N	0.64 ± 0.12	0.42 ± 0.18	0.79 ± 0.14

a mean $ARV = 0.38 \pm 0.21$ and $COR = 0.62 \pm 0.13$ using the Rectified voltage as input. When the Siscoe voltage is used as input the mean AL $ARV = 0.41 \pm 0.16$ and $COR = 0.52 \pm 0.15$. The Newell input coupling function has the best *AL* performance of the three with a mean $ARV = 0.33 \pm 0.17$ and $COR = 0.64 \pm 0.12$.

The best *Dst* prediction is obtained from the Rectified input voltage with a mean $ARV = 0.37 \pm 0.27$ and $COR = 0.80 \pm 0.12$. For Siscoe voltage input the mean *Dst* $ARV = 0.42 \pm 0.23$ and $COR = 0.77 \pm 0.13$. The mean *Dst* $ARV = 0.54 \pm 0.39$ and $COR = 0.79 \pm 0.14$ results for the Newell input show that the Newell

input coupling function did not perform as well as the Rectified and Siscoe input. However, the mean *Dst* COR for all three input functions are very similar with only a few percent differences.

Table 4.3 also shows the direct correlation coefficient of the *AL* index with the input solar wind driving voltage (calculated from data) in the third column. The direct correlation of *Dst* index with the input driving voltage is not shown as the model *Dst* will always have a higher correlation with the *Dst* index data than the input coupling function, because the *Dst* a time integrated index. The mean direct correlation coefficient for the *AL* is $\text{COR} = 0.40 \pm 0.20$ with the Rectified, $\text{COR} = 0.37 \pm 0.18$ for the Siscoe input, and $\text{COR} = 0.42 \pm 0.18$ for the Newell input. The model *AL* correlates with the *AL* index data at least one standard deviation better than a direct correlation of each coupling function with the *AL* data.

The mean RMSE of the events is shown in Table 4.4 and the values confirm the ARV and COR comparisons of the three coupling functions. The *AL* prediction has an average $\text{RMSE} = 111.5 \pm 39.5$ nT, 126.1 ± 52.4 nT, and 125.2 ± 45.5 nT for the Newell, Rectified, and Siscoe input voltages respectively. For the *Dst* prediction the average $\text{RMSE} = 9.8 \pm 3.4$, 10.7 ± 4.0 , and 11.9 ± 6.9 nT for the Rectified, Siscoe, and Newell coupling functions.

Storm prediction can also be assessed from the statistical decision process perspective. Using the storm event selection criteria we define “correct” to mean the data $Dst \leq -50\text{nT}$ and the model was also $Dst \leq -50\text{nT}$. The type I error or “false negative” means the data $Dst \leq -50\text{nT}$ and the model *Dst* was not $\leq -50\text{nT}$. The type II error or “false positive” means the data was not $Dst \leq -50\text{nT}$ and the

Table 4.4: Mean values of the Root Mean Squared Error (RMSE) of Real-Time WINDMI model results with the *AL* and *Dst* index are shown in the second and third columns. The RMSE is calculated using Equation 4.3 in Section 4.3.

Feb. 2006 - Aug. 2008 Selected Events, Mean RMSE		
Input	Mean <i>AL</i> RMSE	Mean <i>Dst</i> RMSE
<i>Rectified</i> V_{sw}^{Bs}	123.2 \pm 52.4	9.8 \pm 3.4
<i>Siscoe</i> V_{sw}^S	126.1 \pm 45.5	10.7 \pm 4.0
<i>Newell</i> V_{sw}^N	111.5 \pm 39.5	11.9 \pm 6.9

model *Dst* was ≤ -50 nT. The statistical *Dst* decisions are evaluated from Table 4.1 and for the Rectified or Siscoe input there are 4/15 (73.3%) correct, 11/15 (26.7%) false negatives, and 0/15 (0%) false positives. For the Newell input there are 8/15 (53.3%) correct, 7/15 (46.7%) false negatives, and 0/15 (0%) false positives.

WINDMI model results can be compared with a simple persistence model in which the prediction is the *AL* or *Dst* value from the previous hour. The persistence *Dst* prediction performs very well with an average ARV = 0.06 ± 0.04 and COR = 0.94 ± 0.03 . These results are consistent with the *Dst* measuring the time integrated strength of the large scale ring current which is not strongly influenced by chaotic magnetosphere processes. The *AL* persistence prediction does not perform as well as the WINDMI model with an average ARV = 0.52 ± 0.27 and COR = 0.43 ± 0.16 . The *AL* index measures the smaller scale electrojet currents which are dependent on magnetosphere turbulence and the solar wind-magnetosphere dynamic interaction and therefore the *AL* is better characterized by the WINDMI model.

4.5 Real-Time WINDMI Results: 14-18 December 2006

ACE solar wind data for the largest event, 14-18 December 2006, is shown in Figure 4.1. The Rectified, Siscoe, and Newell input driving voltages for this period are shown in Figure 4.2, and the Real-Time WINDMI results, AL , Dst , and symH data are shown in Figure 4.3. This event has also been selected by the GGCM (Geospace General Circulation Model) Metrics and Validation Focus Group of the GEM (Geospace Environment Modeling) workshop as a targeted event modeling challenge with focus on the inner magnetospheric dynamics using data from magnetopause crossings by geosynchronous satellites.

A halo CME occurs at 0254 UT on 13 December with a projected speed of 1774 km/s and is accompanied by an X3.4 flare [32, 30]. ACE solar wind data for this period is shown in Figure 4.1. There is a shock at 1352 UT on 14 December in the ACE number density and velocity data with a speed of 1030 km/s [30]. The magnetopause standoff distance computed using the Shue et al. [42] equation and ACE data is shown in Figure 4.4. Sudden storm commencement occurs at 1414 UT on 14 December and the Dst reached -146 nT at 0730 UT (the midpoint of the hourly Dst interval) on 15 December. In recent years a new index, symH, representing ring current development with a 1-minute temporal resolution, has become available [21] and can be used as a higher-resolution version of Dst [58]. On 15 December, minimum symH reached -211 nT at 0056 UT and hourly-averaged symH -191 nT at 0030 UT. The minimum ΔH values at the Earth due to the ring current in WINDMI are -180/-193/-228 nT for the Rectified/Siscoe/Newell driver voltages at 0914/0926/0924 UT, respectively, on 15 December. These values are very close to

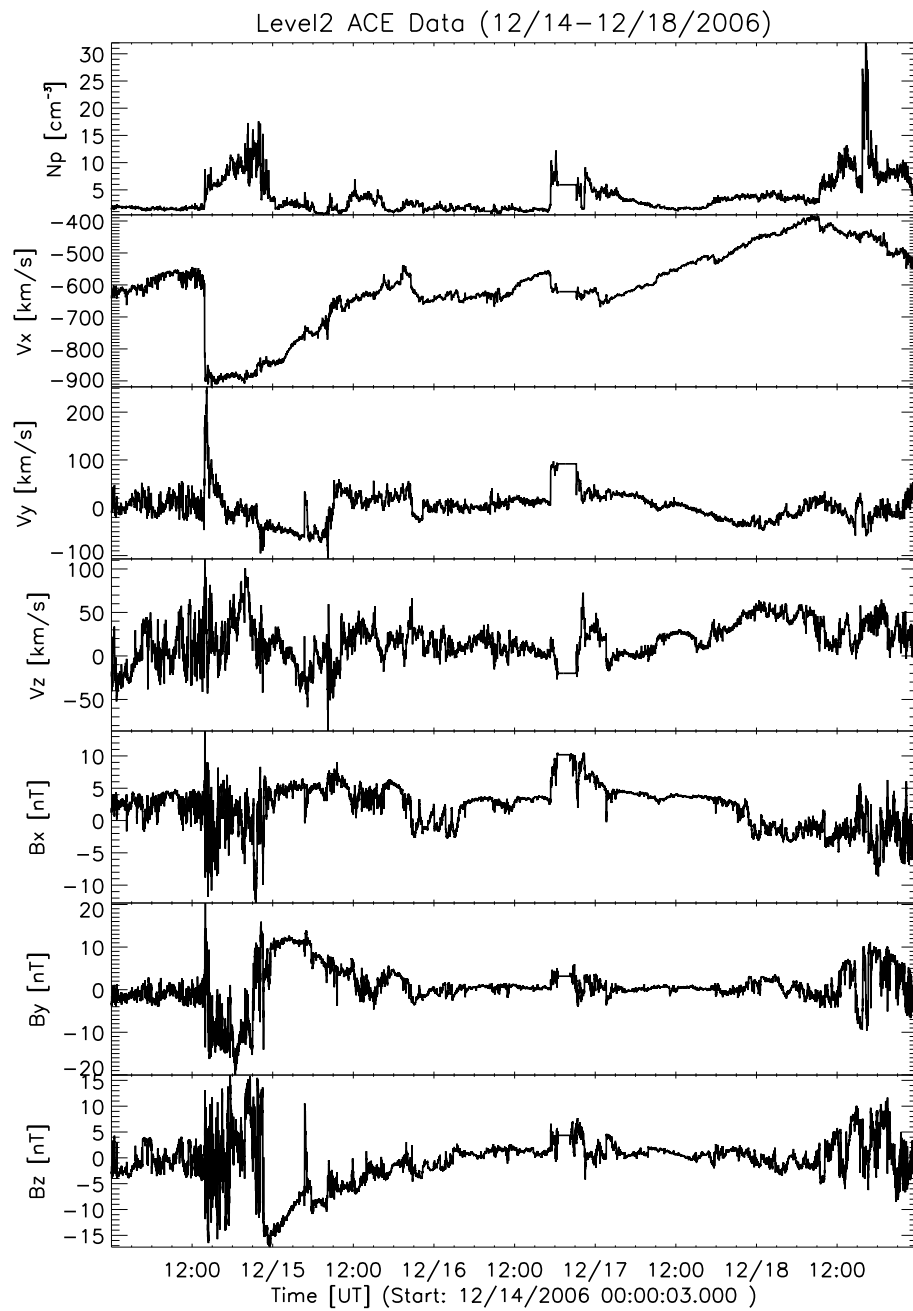


Figure 4.1: ACE solar wind number density, velocity, and interplanetary magnetic field data for 14-18 December 2006 in GSM coordinates show a shock at 1352 UT on 14 December with a speed of 1030 km/s.

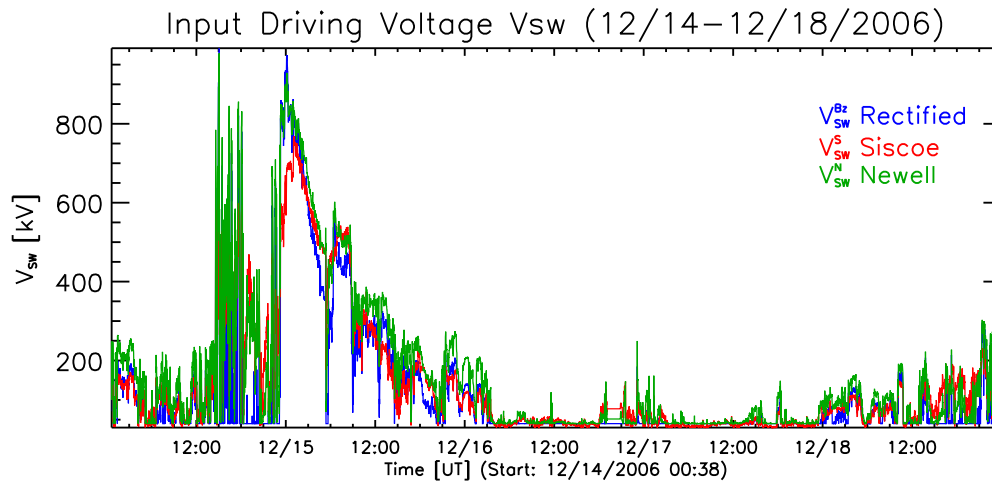


Figure 4.2: Rectified V_{sw}^{Bs} (blue), Siscoe V_{sw}^S (red), and Newell V_{sw}^N (green) input solar wind driving voltages for 14-18 December 2006.

the observed minimum symH but are significantly lower than the observed minimum *Dst*. In addition, the minima in *Dst* and symH occurred 1.75-2 hours and 8.5 hours earlier, respectively, than the WINDMI minimum *Dst* prediction. As a result, the ring current was well into its recovery phase by the time WINDMI predicted peak ring current energy content. The observed earlier recovery of the symH and *Dst* compared to WINDMI is most likely due to a drop in the nightside plasma sheet density (ring current source population) observed by the LANL geosynchronous satellites [data from CDAWeb, courtesy of LANL]. Decreases in plasma sheet density on the nightside are known to be a contributing factor at times in the ring current decay, such as in the 25 September 1998 magnetic storm[27, 29, 22]; but these variations are not represented in WINDMI. This drop in plasma sheet density could be the cause of the observed *Dst* beginning rapid recovery while WINDMI and all

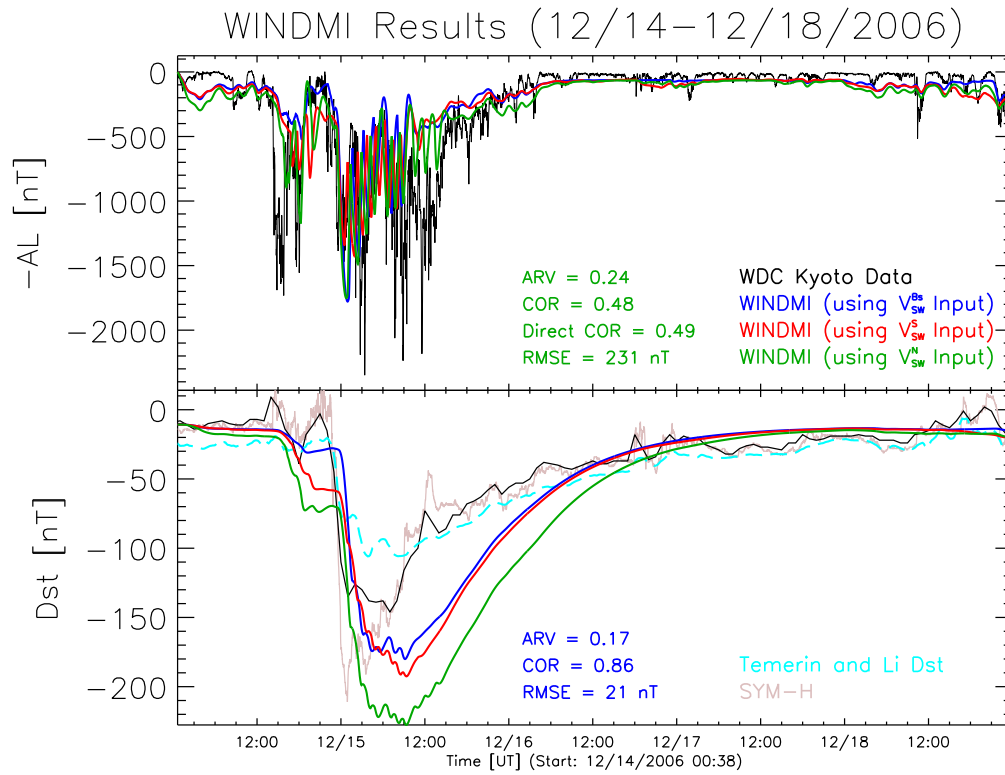


Figure 4.3: Real-time WINDMI AL and Dst results for 14–18 December 2006. Model results using as input the Rectified voltage V_{sw}^{Bs} are shown in blue, the Siscoe voltage V_{sw}^S in red, and Newell voltage V_{sw}^N in green. WDC Kyoto provisional AL and Dst data is shown in black, and the SYM-H data in gray.

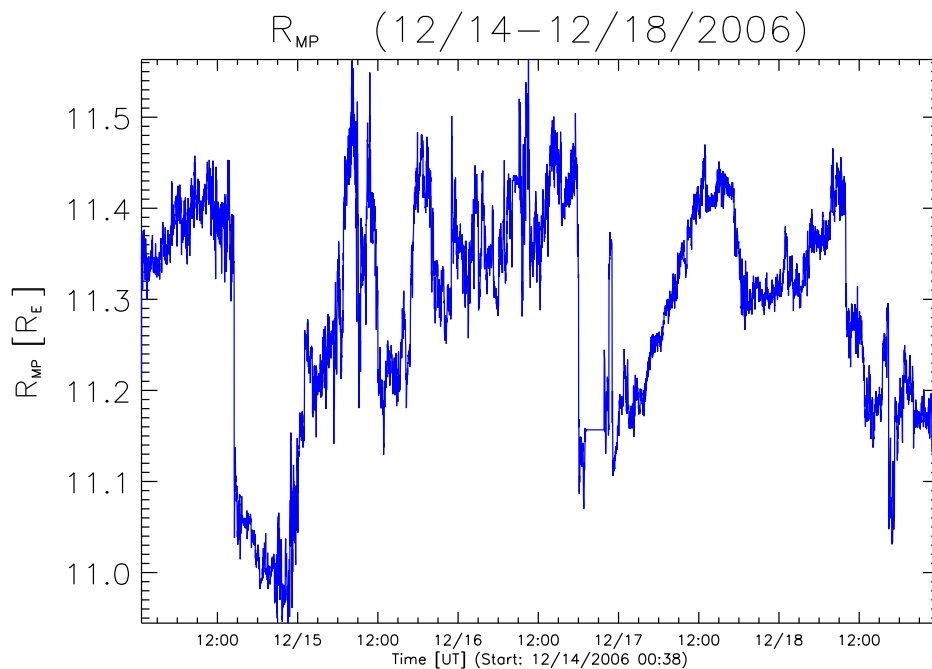


Figure 4.4: Magnetopause standoff distance R_{mp} computed using the Shue et al. [42] equation and ACE data for 14-18 December 2006

other ring current models to predict a continuing growth of the ring current based on the upstream solar wind parameters of strong southward IMF.

The AL index shows much activity with large negative spikes of -1690 nT, -1732 nT, and -1555 nT on 14 December at 1451 UT, 1549 UT, and 1802 UT, and larger negative spikes of -2191 nT, -2349 nT, -2237 nT, and -2183 nT on 15 December at 0246 UT, 0324 UT, 0852 UT, and 1135 UT. WINDMI missed the AL spike at 1451 UT on 14 December associated with shock arrival. This is illustrated in Figure 4.5 which is a closer look at the magnetopause standoff distance on 14 December along with the AL data. WINDMI predicted the timing and magnitude of next

two AL spikes quite well. But then underpredicted the magnitude of the larger *AL* spikes of substorm activity on 15 December which are associated with a strong spike in northward IMF during a strong, steady southward IMF. The *AL* and *AU* data for 15 December are shown in Figure 4.6. This is particularly interesting because the *AL* spikes at 0324 UT and 0852 UT on 15 December both preceded large drops in nightside plasma sheet density that contributed to intervals of rapid ring current recovery seen in the *Dst* not reproduced in WINDMI and other models. The severe substorm on 15 December triggered by the strong northward IMF spike appears to have interrupted the supply of plasma sheet material to the inner magnetosphere and changes the dynamics of the magnetotail. If the magnetotail is shortened or distorted by the ejected plasmoid the subsequent substorms could be triggered by a method different from the triggers and parameterizations included in WINDMI. Such as an internally-driven periodic response of the magnetosphere set off by the first triggered substorm, which has been proposed for the 25 September 1998 event.

There is ongoing work with collaborators in the community targeted study of the 14-18 December 2006 event to see how (1) MHD models evolve throughout this and similar events, and (2) if MHD models coupled with kinetic ring models reproduce the *Dst* behavior, and (3) if these models capture the substorms after the most severe one.

4.6 Discussion and Conclusions

For the time period between February 2006 to September 2008, twenty-two storm and/or substorm events are studied based on forecasts with the Real-Time

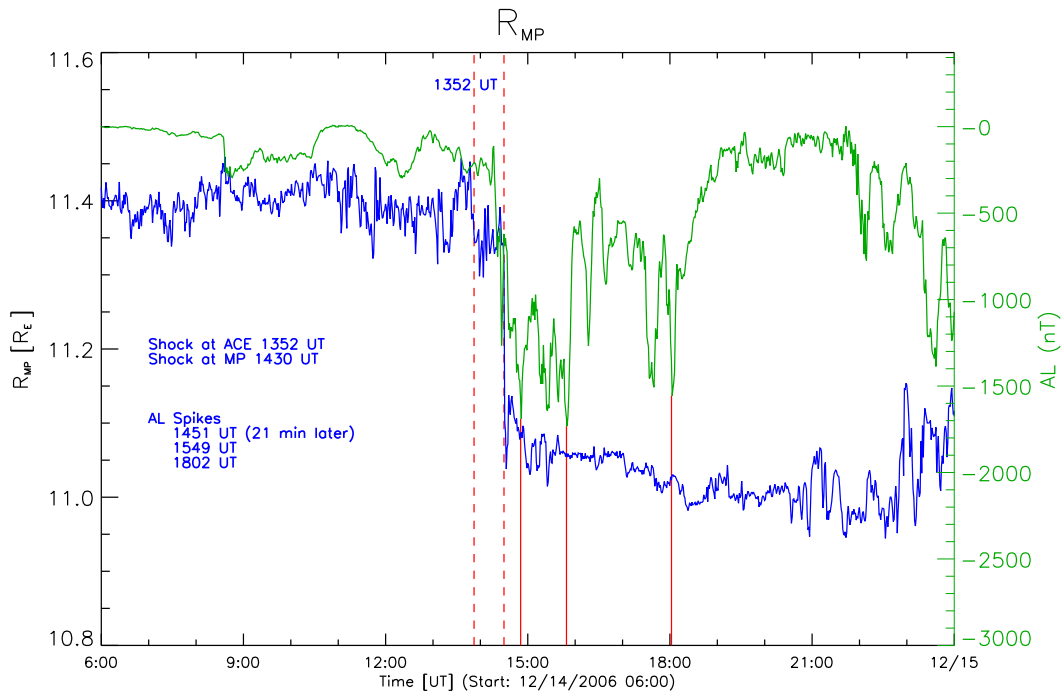


Figure 4.5: Zoom in on magnetopause standoff distance shown in Figure 4.4 for 14 December. The shock times at ACE are marked by dotted red lines and the AL spikes by solid red lines. The first AL spike not captured by WINDMI is thought to be a result of the sudden dayside compression associated with shock arrival.

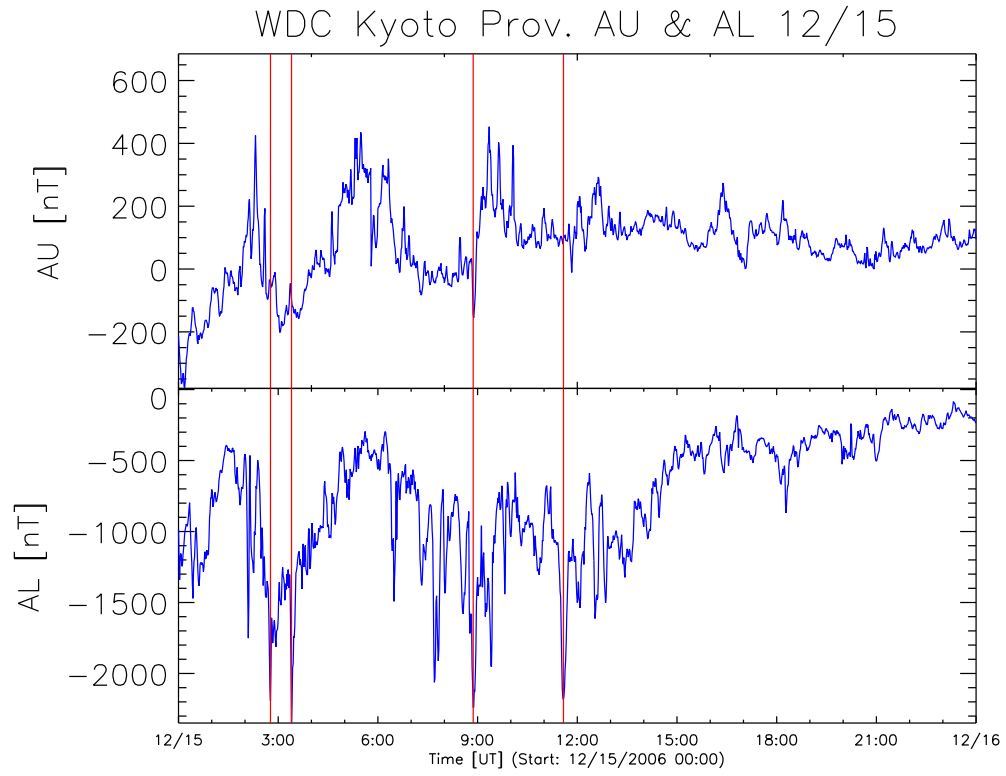


Figure 4.6: *AL* and *AU* data for 15 December with *AL* spikes marked by solid red lines with values -2191 nT, -2349 nT, -2237 nT, and -2183 nT at 0246 UT, 0324 UT, 0852 UT, and 1135 UT.

WINDMI model. The model has been working reliably for two years with an email alert system set to a threshold of -50 nT and -400 nT for the predicted *Dst* and *AL* respectively.

The performance of the model is evaluated for twenty-two events (see Table 4.1) with the Average Relative Variance (ARV), correlation coefficient (COR), and Root Mean Squared Error (RMSE) by comparing model results to *AL* and *Dst* data from WDC Kyoto. The Newell input function yielded the best model *AL* predictions by all three measures (mean ARV, COR, and RMSE), followed by the Rectified, then Siscoe input functions. Model *AL* predictions correlate at least one standard deviation better with the data than a direct correlation between the input coupling functions and the *AL* index.

The Rectified input has the best mean *Dst* ARV by a percent difference of 13% and 37% from the mean *Dst* ARV of the Siscoe and Newell inputs respectively. The mean *Dst* COR and RMSE measures do not readily distinguish between the three input coupling functions. The solar wind input driver which produces the best *Dst* and *AL* WINDMI model predictions are different for each index. This suggests that different solar wind-magnetosphere coupling physics may be responsible for producing the electrojet and ring current.

Spencer et al. [49] show that the Newell input function yields slightly better *Dst* results and the Rectified input slightly better *AL* results when used with an optimized parameter set. However, their study was for large geomagnetic activity of long duration (15-24 April 2002) for which the input coupling functions were evaluated after WINDMI model parameter optimization on a large previous event

(3-7 October 2000).

Chapter 5

Dayside WINDMI Model

5.1 Introduction

The dynamics of the dayside magnetosphere is determined by the upstream solar wind, the bow shock, and the downstream sub-Alfvénic and subsonic fast flows in the magnetosheath around the magnetopause. The WINDMI model discussed in Section 2 describes the coupling of the solar wind to the nightside inner and outer magnetosphere system. The model set forth here describes how plasma energy flows from the solar wind driver through the dayside magnetopause into the magnetosphere. The oscillations of the dayside magnetopause boundary from sudden changes in solar wind properties is derived. The system describes three semi-global Alfvén oscillations of the dayside plasma.

The sudden storm commencement as observed in the Dst arising from the Chapman-Ferraro magnetopause current at dayside magnetopause boundary is modeled. The addition of this term to the tail current contribution to the Dst derived from WINDMI yields a more detailed WINDMI Dst model.

The new dayside model gives six ordinary differential equations that describe the dynamics from the upstream solar wind driver through this region. Dayside WINDMI is divided into the bow shock current loop, the dayside region 1 field aligned current, the dayside region 2 field aligned current, and the Chapman-Ferraro

current. The AU index measures the strength of the dayside eastward auroral electrojet and can be modeled by dayside WINDMI from the model dayside region 1 current.

5.2 Dayside Magnetopause Dynamics

Dayside magnetic reconnection has a strong influence on the dynamics of the entire magnetosphere. The solar wind pressure is the principally dynamic quantity given by $P_{\text{sw}} = \rho_{\text{sw}}v_{\text{sw}}^2 + B_{\text{IMF}}^2/2\mu_0$ and exerts an inward force on the dayside magnetopause area. The local conservation form of the momentum flow from Newton's second law is given by

$$\partial_t(\rho\mathbf{v}) + \nabla \cdot \left[\rho\mathbf{v}\mathbf{v} + \left(p + \frac{B^2}{2\mu_0} \right) \mathbf{I} - \frac{\mathbf{B}\mathbf{B}}{\mu_0} \right] = 0 \quad (5.1)$$

where ρ is the mass density. To derive the dynamics of the magnetopause boundary $R_{\text{mp}}(t)$ the local momentum conservation form of equation 5.1 is projected on to the shell volume $A_{\text{mp}} \Delta r_{\text{mp}}$ containing the magnetopause, where Δr_{mp} is the effective magnetopause width. Equation 5.1 is integrated over the volume, using the ideal frozen-in law for the plasma velocity \mathbf{v} and Gauss's law to derive

$$E_\phi + v_\perp B = 0 \quad (5.2)$$

$$\rho \frac{\partial}{\partial t} v_\perp = \rho \frac{\partial}{\partial t} \left(\frac{-E_\phi}{B} \right). \quad (5.3)$$

The width l_ϕ is defined as $rd\phi$, the flux $d\Psi = rd\phi B_\theta = l_\phi r B_\theta$, and the volume element becomes $d^3x = drl_\phi ds = d\Psi ds/B$.

$$\int d^3x \rho \frac{\partial v_r}{\partial t} = \int d\Psi \frac{ds}{B_\theta} \rho \frac{\partial}{\partial t} \left(\frac{-E_\phi}{B} \right) \quad (5.4)$$

A more general form of Eq. 5.2 follows from $\nabla\phi \cdot \mathbf{E} = -\nabla\phi \cdot \mathbf{v} \times \mathbf{B} = -\mathbf{v} \cdot (\mathbf{B} \times \nabla\phi) = \mathbf{v} \cdot \nabla\Psi(\nabla\phi)^2 = v^\Psi(\nabla\phi)^2$, where $v^\Psi = l \sin\theta E_\phi = \Delta V(t)$ is the contravariant component of the MHD flow velocity \mathbf{v} . Thus, we see that the contravariant component of the velocity v^Ψ is equal to the voltage drop $V_{\text{mp}}(t) = E_\phi l_\phi$ of area A_{mp} and thickness Δr_{mp} . For a dayside eastward electric field the accelerated mass follows

$$\int_{\Omega_{\text{mp}}} d^3x \rho \frac{\partial v_\perp}{\partial t} = d\Psi \int \frac{ds}{B} \rho \frac{\partial}{\partial t} \left(\frac{\Delta V}{l_\phi} \right) \quad (5.5)$$

$$d\hat{\Psi} = dr B \quad (5.6)$$

$$\int_{\Omega_{\text{mp}}} d^3x \rho \frac{\partial v_\perp}{\partial t} = d\hat{\Psi} \int \frac{ds}{B^2} \rho \frac{dV}{dt}. \quad (5.7)$$

The plasma capacitance is expressed in terms of the plasma mass density $\rho(r, \theta)$ as $C_{\text{mp}} = \int \frac{ds}{B_\phi^2} \rho$ where the surface integral is along a constant flux tube.

Next the integral of the divergence of the momentum stress tensor over the volume Ω_{mp} is considered. The flux per unit l_ϕ is defined as $\hat{\Psi} = \Psi/l_\phi$ in Equation 5.6. The force acting on the plasma in the magnetopause shell of volume Ω_{mp} is

$$\begin{aligned} \int_{\Omega_{\text{mp}}} d^3x \nabla \cdot \overleftrightarrow{\mathbf{T}} &= \int_{\partial\Omega=S_2-S_1} d^2x \frac{\nabla \hat{\Psi}}{B} \cdot \overleftrightarrow{\mathbf{T}} \\ &= \int_{S_2(\text{sw})} ds (r \sin\theta d\phi) \left[\rho v_{\text{sw}}^2 + \left(p + \frac{B_{\text{IMF}}^2}{2\mu_0} \right) - \frac{B_n^{\text{sw}} B_n^{\text{sw}}}{\mu_0} \right] \\ &\quad - \int_{S_1(\text{dip})} ds dl_\phi \left(p + \frac{B_\theta^2}{2\mu_0} \right) - \int_{S(\text{west})} ds \Delta r_{\text{mp}} \rho v_r v_\phi \\ &\quad - \int_{S(\text{east})} ds \Delta r_{\text{mp}} \rho v_r v_\phi \end{aligned} \quad (5.8)$$

where the B_n^{sw} only has nonvanishing for southward IMF due to reconnection.

The magnetopause flow directly proportional to the incident dynamic pressure and it is divergent and tangential to the magnetopause surface such that only

magnetic and thermal pressure components remain. The last two terms represent the loss of this dynamics pressure to the divergence of the momentum flux out of the west and east sides S (west) and S (east) of the dayside magnetopause shell. Following Kivelson and Russell [23] the numerical quantity κ is used to estimate the amount the pressure has been diminished by the divergence of the flow. The value of $\kappa = 0.844$ corresponds to a 15% decrease of the solar wind dynamic pressure. The compression factor a is also introduced due to the contribution of other current systems to the magnetic field at the magnetopause and it has been determined empirically to be 2.44. This means that the magnetic pressure of the magnetopause is about 2.44 times that expected for a vacuum field at that distance.

The integral over Ω_{mp} reduces to the boundary flows around the surfaces $\partial\Omega_{\text{mp}}$ of Ω_{mp} . The force-acceleration equation for the shell of width Δr_{mp} and area A_{mp} of \mathbb{R}^3 is projected to the six surfaces of \mathbb{R}^2 . The mean value theorem is applied to each face to obtain the projection of the momentum balance equation as two ordinary differential equations. The results give mechanical equations for $R_{\text{mp}}(t)$ and $v_{\text{mp}}(t) = dR_{\text{mp}}/dt$ including a frictional drag to v_{mp} in the acceleration to account for the loss of energy radiated into ULF waves by the oscillations of the magnetopause dipole moment. The velocity of the magnetopause boundary driven

by the solar wind is given by the pair of equations

$$\frac{dR_{\text{mp}}}{dt} = v_{\text{mp}}(t) \quad (5.9)$$

$$\begin{aligned} M_{\text{mp}} \frac{dv_{\text{mp}}}{dt} &= A_{\text{mp}} \left(\frac{R_{\text{mp}}(t)}{R_E} \right)^2 \times \\ &\left[\left(\frac{(aB_0)^2}{2\mu_0} \left(\frac{R_E}{R_{\text{mp}}(t)} \right)^6 \right) - \left(\kappa \rho v_{\text{sw}}^2 + \frac{B_{\perp\text{sw}}^2}{2\mu_0} \right) \right] - \nu_{\text{ULF}} M_{\text{mp}} v_{\text{mp}} \quad (5.10) \\ &= -\frac{\partial U_{\text{mp}}}{\partial R} - \nu_{\text{ULF}} M_{\text{mp}} v_{\text{mp}} \end{aligned}$$

where A_{mp} is the effective nose area $A_{\text{mp}} \approx \alpha_{\text{mp}} R_{\text{mp}}^2(t)$ with $\alpha_{\text{mp}} \approx 0.1$ to 0.2 . The parameters which are the coefficients of the differential equations are listed in Table 5.1. The mechanical potential energy $U_{\text{mp}}(R)$ of the magnetopause layer is given by

$$U_{\text{mp}}(R) = \frac{A_{\text{mp}}}{3} \left[\left(\frac{B_0^2}{2\mu_0} \frac{R_E^4}{R_{\text{mp}}^3(t)} \right) + \frac{p_{\text{mp}}(t) R_{\text{mp}}^3(t)}{R_E^2} \right]. \quad (5.11)$$

The potential energy function describes a deep, nonlinear potential well for the stable oscillations of the magnetopause. Excursions of the magnetopause are large only during periods of very low solar wind dynamic pressure. When $U_{\text{mp}}=0$ then the magnetopause boundary velocity becomes $v_{\text{mp}} = v_{\text{mp}}(0)e^{-\nu_{\text{ULF}}t}$, such that the kinetic energy of the magnetopause decays away as radiating ULF waves.

The ACE solar wind data for the 19-23 November 2007 event is shown in Figure 5.1. The dynamics of Equations 5.9 and 5.10 for $R_{\text{mp}}(t)$ and $v_{\text{mp}}(t)$ are shown in Figure 5.2 for the 19-23 November 2007 event.

Table 5.1: WINDMI dayside parameters for the $(R_{\text{mp}}(t), v_{\text{mp}}(t))$ system (Equations 5.9 and 5.10).

Parameter	Value	Description
Δl_ϕ	$10 R_E$	Width of region 1 current loop “triangle” on magnetopause boundary.
Δr_{mp}	$2 R_E$	Width of plasma shell over which force equation is projected.
C_{mp}	10000 F	Plasma capacitance of the magnetopause $C_{\text{mp}} = \int \frac{ds \rho}{B_\theta^2}$
A_{mp}	$10 R_E^2$	Area of the region 1 current loop which forms the dayside R1 “triangle” plasma shell.
ρ_{mp}	$2 \times 10^{-20} \text{ kg m}^{-3}$	Mass density of magnetopause shell.
M_{mp}	$10^3\text{-}10^4 \text{ kg}$	Total mass enclosed in the magnetopause shell.
B_0	30000 nT	Magnetic field at the Earth’s surface on the magnetic equator.
Δz	$20 R_E$	Height of ampere loop over which the magnetic field jumps (used in the calculation of the the Chapman-Ferraro current)

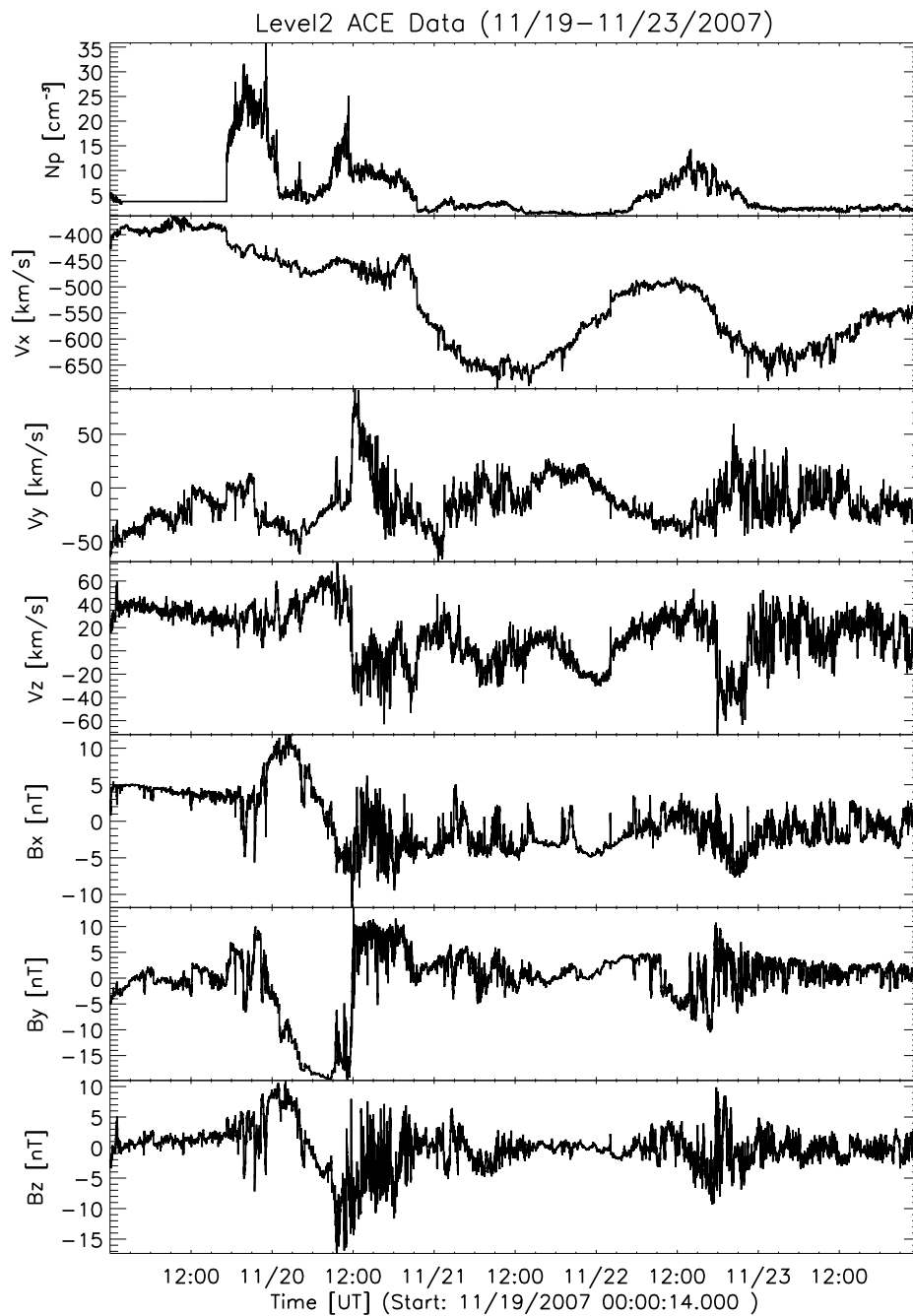


Figure 5.1: ACE solar wind number density, velocity, and interplanetary magnetic field data for 19-23 November 2007 in GSM coordinates.

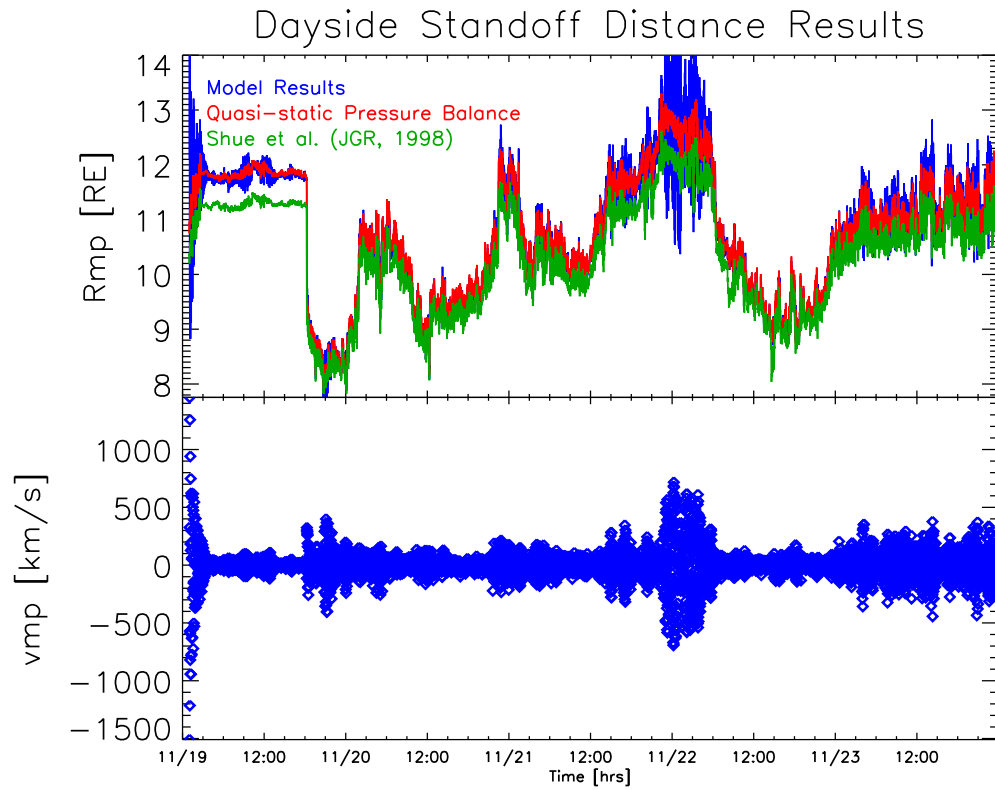


Figure 5.2: 19-23 November 2007: The dynamics of Equations 5.9 and 5.10 for the magnetopause shell at $R_{mp}(t)$ and the radial velocity $v_r(t) = dR_{mp}(t)/dt$.

5.3 Sudden Storm Commencement

The sudden positive *Dst* jump (increase of the Earth's surface magnetic field) known as sudden storm commencement (see Section 1.5.1) is due to the strengthening of the Chapman-Ferraro magnetopause current (see Section 1.4.2).

We define the Chapman-Ferraro current $I_{\text{CF}}(t)$ as

$$I_{\text{CF}}(t) = \Delta z(B_{\text{dip}} - B_z^{\text{IMF}})/\mu_0 = \Delta z(B_0 R_E^3/R_{\text{mp}}^3(t) - B_z^{\text{IMF}})/\mu_0. \quad (5.12)$$

The perturbation ΔB_{CF} can be estimated by determining the magnetic moment \mathbf{M}_{CF} of the current system,

$$\Delta \mathbf{B}_{\text{CF}} = \frac{\mu_0}{4\pi} \frac{\mathbf{M}_{\text{CF}}}{(R_{\text{mp}}(t))^3}, \quad (5.13)$$

where $\mathbf{M}_{\text{CF}} = \mathbf{M}_{\text{CF}}^{\text{N}} + \mathbf{M}_{\text{CF}}^{\text{S}}$ is the vector sum of the CF-magnetic moments from the northern and southern current loops. $R_{\text{mp}}(t)$ is the location of the magnetopause that carries \mathbf{M}_{CF} from Equation 5.9. If we assume the Chapman-Ferraro magnetic dipole vectors make an angle of 45° with the equatorial plane and the magnitude of the current $I_{\text{CF}}(t)$ and area A_{mp} is the same for both hemispheres we have $\mathbf{M}_{\text{CF}} = \sqrt{2}M_{\text{CF}}^{\text{N}}\hat{\mathbf{e}}_z = \sqrt{2}A_{\text{mp}}I_{\text{CF}}(t)\hat{\mathbf{e}}_z$. The Chapman-Ferraro magnetic perturbation at the center of the Earth is

$$\Delta \mathbf{B}_{\text{CF}} = \hat{\mathbf{e}}_z \frac{\mu_0}{4\pi} \frac{\sqrt{2}A_{\text{mp}}I_{\text{CF}}(t)}{(R_{\text{mp}}(t))^3}. \quad (5.14)$$

5.4 Tail Current Contribution to the Dst

The magnetotail configuration and current is discussed in Section 1.4.3. As mentioned in Section 1.5.3, during geomagnetic activity the the tail current can produce a northward magnetic perturbation at the center of the Earth which is measured as a decrease of the Dst . Turner et al. [56] show that up approximated one quarter of the Dst decrease is due to the effect the tail current.

The magnetic field from the tail current $\Delta\mathbf{B}_{\text{tail}}(I)$ can be computed from the WINDMI magnetotail current from

$$\Delta B_{z,\text{tail}}(I) = - \int_{r_1}^{r_2} \frac{I(x')(x')}{(x'^2 + z^2)^{3/2}} dx' \quad (5.15)$$

where magnetotail current distribution is estimated by $I(x') = I(t)e^{-\frac{(x'-x_{\text{max}})^2}{(x_{\text{max}})^2}}$ and the integration limits $r_1 \approx 6R_E$ and $r_2 \approx 150R_E$ are the inner and outer boundaries of the magnetotail. The distance $x_{\text{max}} \approx 15R_E$ is the location of the current density profile maximum from MHD model runs.

5.5 Improved Dst Modeling

Combining the results of Sections 5.3 and 5.4 with the WINDMI Dst computed from the Dessler-Parker-Sckopke relation given in Equation 1.18, the model $\Delta\mathbf{B}$ for the Dst becomes

$$\Delta\mathbf{B} = \Delta\mathbf{B}_{\text{rc}}(W_{\text{rc}}) + \Delta\mathbf{B}_{\text{tail}}(I) + \Delta\mathbf{B}_{\text{CF}}(I_{\text{CF}}). \quad (5.16)$$

5.6 Dayside WINDMI Model

The existence and general properties of the region 1 and region 2 field aligned currents were verified by Iijima [20] by measurements of the associated magnetic fields. The methodology used is the same as on the nightside magnetosphere described in Section 2.2. Figure 5.3 shows the dayside view along the Sun-Earth line of the geometry of the region 1 field-aligned current, region 2 field aligned current, ring current, and magnetopause current loops corresponding to the nightside current systems shown in Figure 1.3. The current loops are not unique and extended models could well be needed with more loops and nodes.

Dynamics of the dayside region 1 current I_1^d is due to both the polar cap potential V_{pc} driven by the solar wind and the bow shock dynamics with current loop I_{bs} . The polar cap potential V_{pc} is defined from the Hill et al. [14] equation for the transpolar potential

$$V_{pc} = \frac{V_{sw}^S \Phi_S}{V_{sw}^S + \Phi_S}. \quad (5.17)$$

where V_{sw}^S is the Siscoe coupling function from Equation 2.11 and Φ_S is the saturated value of the transpolar potential. The bow shock voltage V_{bs} maps from the solar wind and is similar to Equation 2.10 for the rectified driving voltage. However, at the bow shock, the direction of the current I_{bs} changes with the interplanetary magnetic direction, giving a bow shock dynamo voltage of the form

$$V_{bs} = -L_y^{bs} v_{sw} B_z^{IMF} \quad (5.18)$$

The bow shock is a powerful generator with the power $V_{\text{bs}}I_{\text{bs}} < 0$. When B_z^{IMF} changes from northward to southward V_{bs} and I_{bs} both change sign such that the Poynting flux S_{bs} remains inward to the shock. The effective length L_y^{bs} over which the voltage is generated is larger than the $10 R_E$ used for the nightside coupling. The compression current for the perpendicular component of the IMF is

$$(r_{\text{bs}} - 1)\Delta z_{\text{bs}}B_z^{\text{IMF}}/\mu_0 \quad (5.19)$$

This network of the dayside bow shock current, region 1 field aligned current, region 2 field aligned current forms a system of differential equations as follows

$$L_{\text{bs}}\frac{dI_{\text{bs}}}{dt} = V_{\text{sw}} - V_{\text{bs}} \quad (5.20)$$

$$C_{\text{bs}}\frac{dV_{\text{bs}}}{dt} = I_{\text{bs}} - I_1^{\text{d}} - \frac{(r_{\text{bs}} - 1)\Delta z_{\text{bs}}B_z^{\text{IMF}}}{\mu_0} \quad (5.21)$$

$$L_1^{\text{d}}\frac{dI_1^{\text{d}}}{dt} = V_{\text{bs}} - V_1^{\text{d}} + V_{\text{pc}} \quad (5.22)$$

$$C_1^{\text{d}}\frac{dV_1^{\text{d}}}{dt} = I_1^{\text{d}} - I_2 - \Sigma_1V_1^{\text{d}} \quad (5.23)$$

$$L_2^{\text{d}}\frac{dI_2^{\text{d}}}{dt} = V_1^{\text{d}} - V_2 - V_{\text{pc}} \quad (5.24)$$

$$C_2^{\text{d}}\frac{dV_2^{\text{d}}}{dt} = I_2^{\text{d}} - I_{\text{CF}} - \Sigma_2V_2^{\text{d}}. \quad (5.25)$$

The dynamics of Equations 5.20-5.25 is that of three coupled, driven-damped, nonlinear semi-global Alfvén modes of oscillation. The system is driven by the voltage at the bow shock from the solar wind V_{bs} and the Chapman-Ferraro current given by Equation 5.12. The model parameters are shown in Table 5.2 along with approximate equations for the inductances and plasma capacitances.

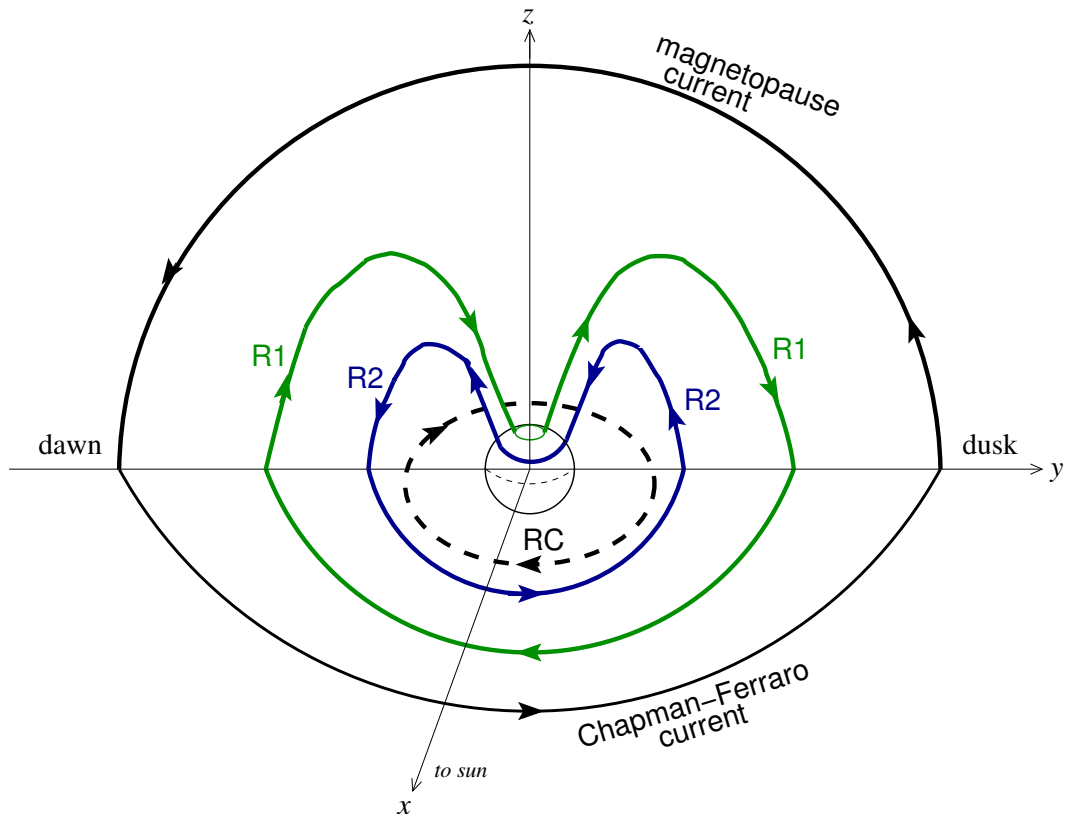


Figure 5.3: Dayside view along the Sun-Earth line of the geometry of the region 1 (R1), region 2 (R2), ring current (RC), and magnetopause current loops corresponding to the nightside current systems shown in Figure 1.3. I_1^d is taken to be proportional to the eastward auroral electrojet. The northward electric field drives a Hall current eastward contributing strongly to the eastward electrojet. The eastward electrojet give the AU geomagnetic index.

Table 5.2: Dayside WINDMI parameters of Equations 5.20-5.25, estimated by physical considerations of a typical state and geometry of the dayside magnetosphere.

Parameter	Value	Description
$L_{\text{bs}} = \mu_0 l_x l_y / l_z$	100 H	Bow shock current loop inductance.
$C_{\text{bs}} = (\rho_{\text{sw}} / B_{\text{sw}}^2)(l_x l_z / l_y)$	1000 F	Bow shock current loop capacitance.
$L_1^{\text{d}} = \mu_0 \pi R_1^2 / l_z$	10 H	Region 1 current loop inductance.
$C_1^{\text{d}} = (\rho_1 / B_1^2)(l_x l_z / l_{y1})$	1000 F	Region 1 current loop capacitance $C_1^{\text{d}} = \int \frac{ds \rho}{B^2}$.
Σ_1	5 mho	Height integrated auroral conductivity for the closure of the region 1 current loop.
$L_2^{\text{d}} = \mu_0 R_{\text{mp}} l_y / l_z$	10 H	Region 2 current loop inductance.
$C_2^{\text{d}} = (\rho_{\text{dp}} / B_{\text{dp}}^2)(l_z R_{\text{mp}} / l_y)$	1000 F	Region 2 current loop capacitance.
Σ_2	2 mho	Auroral conductivity for the lower latitude region 2 current loop.

Preliminary model validation for the surface magnetic perturbation ΔB_{AU} due to the dayside eastward auroral electrojet and the $AU(t)$ data are in progress.

5.7 Discussion

The fluctuations in the solar wind are shown to drive large excursions of the magnetopause position and the dayside region 1 currents that close through the Cowling channel of the dayside auroral zone. The region 1 currents flow eastward in the auroral zone producing the AU geomagnetic index.

Dayside WINDMI reliably produce the dynamics of the magnetopause position $R_{\text{mp}}(t)$ and velocity $v_{\text{mp}}(t) = dR_{\text{mp}}/dt$ and are used to model the magnetopause stand-off distance and Chapman-Ferraro current magnitude. The magnetic pertur-

bation from this current is calculated at the center of the Earth and added to the established WINDMI magnetic perturbation from the model ring current plasma energy. This allows WINDMI to produce a more detailed *Dst* prediction which can give insight into the relative contributions of the magnetosphere current systems to the *Dst* and the physical processes involved.

The validation of model *AU* predictions World Data Center Kyoto are in progress. After model testing and validation the *AU* index prediction from the dayside WINDMI model will be included as part of the Real-Time WINDMI forecast.

The model could possibly be promising for predicting the driving source for the ULF waves in the magnetosphere. Significant power densities are seen in frequencies corresponding to Pc5 and longer period oscillations that arise from the complex structure of the the solar wind driven and the nonlinear response of the magnetopause. Model enhancements in development include adding simple descriptions of the compressional Alfvén cavity modes to the model.

Chapter 6

Conclusions

In this work the use and scope of the WINDMI model has been expanded to the study the effects of interplanetary shocks, to model dayside current systems and the AU index, to include more current systems for Dst modeling, and to produce real-time simulation results as Real-Time WINDMI.

The question of how much interplanetary shock events contribute to the geoeffectiveness of solar wind drivers is assessed through numerical experiments using the WINDMI model, a physics-based model of the solar wind-driven magnetosphere-ionosphere system. Analytic fits to solar wind input parameters allowed shocks and associated shock-sheath plasma to be removed while leaving other features of the solar wind driver undisturbed. Percent changes in WINDMI-derived AL and Dst indices between runs with and without the observed shock and sheath signatures were taken as a measure of its relative contribution to the geoeffectiveness. For two major magnetic storms 15-24 April 2002 and 3-6 October 2000, the IP shock and sheath features contributed significantly to the geoeffectiveness of the solar wind driver. The solar wind-magnetosphere coupling dynamics is found to be most sensitive to variations in the solar wind velocity and interplanetary magnetic field. The magnetic field compressional jump is found to be important to producing the changes in the AL during these two storm intervals.

Real-Time WINDMI, an extension of WINDMI, is used to predict AL and Dst values approximately one hour before geomagnetic substorm and storm events. Subsequently, every ten minutes ground based measurements compiled by WDC Kyoto are compared with model predictions (<http://orion.ph.utexas.edu/~windmi/realtime/>). The performance of the Real-Time WINDMI model is quantitatively evaluated for twenty-two storm/substorm event predictions from February 2006 to August 2008. Measures of prediction performance included the Average Relative Variance (ARV), correlation coefficient (COR), and Root Mean Squared Error (RMSE) by comparing model results to AL and Dst index data. The Newell input function yielded the best model AL predictions by all three measures (mean ARV, COR, and RMSE), followed by the Rectified, then Siscoe input functions. Model AL predictions correlate at least one standard deviation better with the data than a direct correlation between the input coupling functions and the AL index.

The Rectified input has the best mean Dst ARV by a percent difference of 13% and 37% from the mean Dst ARV of the Siscoe and Newell inputs respectively. The mean Dst COR and RMSE measures do not readily distinguish between the three input coupling functions. The solar wind input driver which produces the best Dst and AL WINDMI model predictions are different for each index. This suggests that different solar wind-magnetosphere coupling physics may be responsible for producing the electrojet and ring current.

Real-Time WINDMI was submitted to the Community Coordinated Modeling Center (CCMC: <http://ccmc.gsfc.nasa.gov/>) in October 2008. The CCMC is a multi-agency partnership based at NASA Goddard Space Flight center and provides

the science community with an array of modern space science models in the areas of solar, heliosphere, magnetosphere, and ionosphere/thermosphere. The models are hosted on the CCMC computers and can be run on request through a web interface. We have been collaborating with CCMC research scientists, and in May 2009 Real-Time WINDMI and WINDMI model runs by instant request were released to the public on the CCMC website.

The Real-Time WINDMI validation study is being extended to evaluate the performance of the model using other input driving voltages. The database of Real-Time WINDMI *Dst* predictions is also being compared with other ring current models, and global MHD models which contain different loss and energization processes. The inclusion of sudden storm commencement and tail current magnetic perturbations in WINDMI *Dst* modeling allows the relative contributions of the magnetosphere current systems to the *Dst* and the physical processes involved to be assessed and compared with data and other models. The new dayside WINDMI model has been developed to study the dayside magnetosphere energy dynamics and current systems with resulting ground magnetic perturbations such as the *AU* index.

In modeling the solar wind magnetosphere-ionosphere system, there are some drawbacks in low-dimensional models, such as WINDMI, compared to global MHD models, which have good spatial resolution, and small-scale kinetic models, with good time resolution. However the strengths of WINDMI are in characterizing the global energy dynamics with the fastest simulation speed, while still retaining both the semi-global MHD dynamics and certain kinetic physics terms. These kinetic

physics terms missing include the role of the chaotic ions in the quasi-neutral layer of the central plasma sheet, and the instability trigger for the ballooning interchange mode and the tearing mode in the central plasma sheet. Thus, WINDMI is a good complement to the range of heliospheric physics models.

Appendix

Appendix 1

Geophysical Coordinate Systems

1.1 Geomagnetic Coordinates (MAG)

The z -axis is parallel to the magnetic dipole axis in the geomagnetic coordinate system (MAG) and the y -axis is perpendicular to the geographic poles. The locally tangent spherical polar coordinates are (r, θ, ϕ) and the covariant basis vectors $(\nabla r, \nabla\theta, \nabla\phi)$.

The Jacobian from cartesian to spherical polar coordinates is

$$\begin{aligned} J(x) = \nabla r \times \nabla\theta \cdot \nabla\phi &= \frac{\Delta r}{\Delta r} \hat{\mathbf{e}}_r \times \frac{\Delta\theta}{r\Delta\theta} \hat{\mathbf{e}}_\theta \cdot \frac{\Delta\phi}{r\sin\theta\Delta\phi} \hat{\mathbf{e}}_\phi \\ &= \frac{1}{r^2\sin\theta} \end{aligned} \tag{1.1}$$

1.2 Geocentric Solar Magnetospheric Coordinates (GSM)

The x -axis of the geocentric solar magnetospheric coordinate system (GSM) is from the earth to the sun. The y -axis is perpendicular to the magnetic dipole axis, therefore the $x - z$ plane contains the dipole axis. The positive z -axis is in the same sense as the northern magnetic pole.

Bibliography

- [1] V. Angelopoulos, J. P. McFadden, D. Larson, C. W. Carlson, S. B. Mende, H. Frey, T. Phan, D. G. Sibeck, K.-H. Glassmeier, U. Auster, E. Donovan, I. R. Mann, I. J. Rae, C. T. Russell, A. Runov, X.-Z. Zhou, and L. Kepko. Tail Reconnection Triggering Substorm Onset. *Science*, 321:931–, August 2008. doi: 10.1126/science.1160495.
- [2] D. N. Baker. Effects of the Sun on the Earth’s environment. *Journal of Atmospheric and Solar-Terrestrial Physics*, 62:1669–1681, November 2000.
- [3] L. F. Bargatze, D. N. Baker, R. L. McPherron, and Jr. E. W. Hones. Magnetospheric Impulse Response for Many Levels of Geomagnetic Activity. *J. Geophys. Res.*, 90(A7):6387–6394, July 1985.
- [4] L. F. Bargatze, R. L. McPherron, J. Minamora, and D. Weimer. A new interpretation of Weimer et al.’s solar wind propagation delay technique. *J. Geophys. Res.*, 110(A9):7105, July 2005. doi: 10.1029/2004JA010902.
- [5] R. K. Burton, R. L. McPherron, and C. T. Russell. An empirical relationship between interplanetary conditions and Dst. *J. Geophys. Res.*, 80:4204–4214, November 1975.
- [6] H. V. Cane and I. G. Richardson. Interplanetary coronal mass ejections in the near-Earth solar wind during 1996-2002. *J. Geophys. Res.*, 108:6, April 2003. doi: 10.1029/2002JA009817.

- [7] A.J. Dessler and E. N. Parker. Hydromagnetic theory of geomagnetic storms. *J. Geophys. Res.*, 64:2239–59, 1959.
- [8] I. Doxas, W. Horton, W.T. Lin, S. Seibert, and M. Mithaiwala. A Dynamical Model for the Coupled Inner Magnetosphere and Tail. *IEEE Trans. Plasma Sc.*, 32(4):1443–1448, 2004.
- [9] J. W. Dungey. The Length of the Magnetospheric Tail. *JGR*, 70:1753–1753, April 1965. doi: 10.1029/JZ070i007p01753.
- [10] E. Echer and W. D. Gonzalez. Geoeffectiveness of interplanetary shocks, magnetic clouds, sector boundary crossings and their combined occurrence. *Geophys. Res. Lett.*, 31:9808–+, May 2004. doi: 10.1029/2003GL019199.
- [11] E. Echer, M. V. Alves, and W. D. Gonzalez. Geoeffectiveness of interplanetary shocks during solar minimum (1995-1996) and solar maximum (2000). *Solar Physics*, 221:361–380, June 2004. doi: 10.1023/B:SOLA.0000035045.65224.f3.
- [12] S. Glasstone and R. H. Lovberg. *Controlled Thermonuclear Reactions*. Van Nostrand Company, Princeton, 1960.
- [13] J. T. Gosling, S. J. Bame, D. J. McComas, and J. L. Phillips. Coronal mass ejections and large geomagnetic storms. *Geophys. Res. Lett.*, 17:901–904, June 1990.
- [14] T. W. Hill, A. J. Dessler, and R. A. Wolf. Mercury and Mars - The role of ionospheric conductivity in the acceleration of magnetospheric particles. *GRL*, 3:429–432, August 1976. doi: 10.1029/GL003i008p00429.

- [15] W. Horton and I. Doxas. A low-dimensional energy-conserving state space model for substorm dynamics. *J. Geophys. Res.*, 101(A12):27,223–27,237, December 1996.
- [16] W. Horton and I. Doxas. A low-dimensional dynamical model for the solar wind driven geotail-ionosphere system. *J. Geophys. Res.*, 103(A3):4561–4572, March 1998.
- [17] W. Horton, M. Mithaiwala, E. Spencer, and I. Doxas. WINDMI: A Family of Physics Network Models for Storms and Substorms. In A.T.Y. Lui, Y. Kamide, and G. Consolini, editors, *Multi-Scale Coupling of Sun-Earth Processes*. Elsevier Pub. Co., 2005.
- [18] C.S. Huang, J.C. Foster, G.D. Reeves, G. Le, H.U. Frey, C.J. Pollock, and J.-M. Jahn. Periodic magnetospheric substorms: Multiple space-based and ground-based observations. *J. Geophys. Res.*, 108(A11), 2003. doi: 10.1029/2003JA009992.
- [19] A. Hundhausen. Coronal Mass Ejections. In *The many faces of the sun: a summary of the results from NASA’s Solar Maximum Mission.*, pages 143–200, 1999.
- [20] T. Iijima. *TUTORIAL: Field-Aligned Currents in Geospace: Substance and Significance*, pages 107–130. Magnetospheric Current Systems, 2000.
- [21] T. Iyemori. Storm-time magnetospheric currents inferred from mid-latitude

- geomagnetic field variations. *Journal of Geomagnetism and Geoelectricity*, 42: 1249–1265, 1990.
- [22] V. K. Jordanova, L. M. Kistler, M. F. Thomsen, and C. G. Mouikis. Effects of plasma sheet variability on the fast initial ring current decay. *GRL*, 30(6): 060000–1, March 2003. doi: 10.1029/2002GL016576.
- [23] M.G. Kivelson and C.T. Russell, editors. *Introduction to Space Physics*. Cambridge Univ. Press, 1995.
- [24] A. J. Klimas, D. N. Baker, D. Vassiliadis, and D. A. Roberts. Substorm recurrence during steady and variable solar wind driving: Evidence for a normal mode in the unloading dynamics of the magnetosphere. *JGR*, 99:14855–14862, August 1994. doi: 10.1029/94JA01240.
- [25] A. J. Klimas, D. Vassiliadis, and D. N. Baker. Dst index prediction using data-derived analogues of the magnetospheric dynamics. *JGR*, 103:20435–20448, September 1998. doi: 10.1029/98JA01559.
- [26] A.J. Klimas, D.N. Baker, D.A. Roberts, D.H. Fairfield, and J. Buchner. A Nonlinear Dynamical Analogue Model of Geomagnetic Activity. *J. Geophys. Res.*, 97(A8):12,253–12,266, August 1992.
- [27] J. U. Kozyra, V. K. Jordanova, J. E. Borovsky, M. F. Thomsen, D. J. Knipp, D. S. Evans, D. J. McComas, and T. E. Cayton. Effects of a high-density plasma sheet on ring current development during the November 2-6, 1993, magnetic storm. *JGR*, 103:26285–26306, November 1998. doi: 10.1029/98JA01964.

- [28] X. Li, K. S. Oh, and M. Temerin. Prediction of the AL index using solar wind parameters. *JGR*, 112(A11):6224, June 2007. doi: 10.1029/2006JA011918.
- [29] M. W. Liemohn, J. U. Kozyra, M. F. Thomsen, J. L. Roeder, G. Lu, J. E. Borovsky, and T. E. Cayton. Dominant role of the asymmetric ring current in producing the stormtime dst*. *JGR*, 106:10883–10904, June 2001. doi: 10.1029/2000JA000326.
- [30] Y. Liu, J. G. Luhmann, R. Müller-Mellin, P. C. Schroeder, L. Wang, R. P. Lin, S. D. Bale, Y. Li, M. H. Acuña, and J. . Sauvaud. A Comprehensive View of the 2006 December 13 CME: From the Sun to Interplanetary Space. *ArXiv e-prints*, February 2008.
- [31] P. K. Manoharan, N. Gopalswamy, S. Yashiro, A. Lara, G. Michalek, and R. A. Howard. Influence of coronal mass ejection interaction on propagation of interplanetary shocks. *J. Geophys. Res.*, 109:6109, June 2004. doi: 10.1029/2003JA010300.
- [32] S. M. P. McKenna-Lawlor, M. Dryer, C. D. Fry, Z. K. Smith, D. S. Intriligator, W. R. Courtney, C. S. Deehr, W. Sun, K. Kecskemety, K. Kudela, J. Balaz, S. Barabash, Y. Futaana, M. Yamauchi, and R. Lundin. Predicting interplanetary shock arrivals at Earth, Mars, and Venus: A real-time modeling experiment following the solar flares of 5-14 December 2006. *JGR*, 113(A12):6101–+, June 2008. doi: 10.1029/2007JA012577.
- [33] S. B. Mende, S. E. Harris, H. U. Frey, V. Angelopoulos, C. T. Russell, E. Donovan, B. Jackel, M. Greffen, and L. M. Peticolas. The THEMIS Array of Ground-

based Observatories for the Study of Auroral Substorms. *Space Science Reviews*, page 91, June 2008. doi: 10.1007/s11214-008-9380-x.

- [34] P. T. Newell, T. Sotirelis, K. Liou, and F. J. Rich. A nearly universal solar wind-magnetosphere coupling function inferred from 10 magnetospheric state variables. *J. Geophys. Res.*, 112(A01206), 2007. doi: 10.1029/2006JA012015.
- [35] D. M. Ober, N. C. Maynard, and W. J. Burke. Testing the Hill model of transpolar potential saturation. *J. Geophys. Res.*, 108(A12):1467, 2003. doi: 10.1029/2003JA010154.
- [36] T. P. O’Brien and R. L. McPherron. An empirical phase space analysis of ring current dynamics: Solar wind control of injection and decay. *J. Geophys. Res.*, 105:7707–7720, April 2000. doi: 10.1029/1998JA000437.
- [37] J. L. Phillips, S. J. Bame, W. C. Feldman, B. E. Goldstein, J. T. Gosling, C. M. Hammond, D. J. McComas, M. Neugebauer, E. E. Scime, and S. T. Suess. Ulysses Solar Wind Plasma Observations at High Southerly Latitudes. *Science*, 268:1030–1033, May 1995.
- [38] G.D. Reeves, M.G. Henderson, R.M. Skoug, M.F. Thomsen, J.E. Borovsky, H.O. Funsten, P.C:son Brandt, D.J. Mitchell, J.-M. Jahn, C.J. Pollock, D.J. McComas, and S.B. Mende. Image, polar, and geosynchronous observations of substorm and ring current ion injection. In *Disturbances in Geospace: The Storm-Substorm Relationship*, volume 142 of *Geophysical Monograph*, pages 91–101. AGU, 2003.

- [39] P. H. Reiff and J. G. Luhmann. Solar wind control of the polar-cap voltage. In Y. Kamide and J. A. Slavin, editors, *Solar Wind-Magnetosphere Coupling*, pages 453–476. Terra Sci., Tokyo, 1986.
- [40] G. Rostoker. Geomagnetic Indices. *Reviews of Geophysics and Space Physics*, 10:935, November 1972.
- [41] N. Sckopke. A general relation between the energy of trapped particles and the disturbance field near the Earth. *J. Geophys. Res.*, 71:3125, 1966.
- [42] J.-H. Shue, J. K. Chao, H. C. Fu, C. T. Russell, P. Song, K. K. Khurana, and H. J. Singer. A new functional form to study the solar wind control of the magnetopause size and shape. *JGR*, 102:9497–9512, may 1997. doi: 10.1029/97JA00196.
- [43] D. G. Sibeck and V. Angelopoulos. THEMIS Science Objectives and Mission Phases. *Space Science Reviews*, page 141, June 2008. doi: 10.1007/s11214-008-9393-5.
- [44] K. D. Siebert and G. L. Siscoe. Dynamo circuits for magnetopause reconnection. *Journal of Geophysical Research (Space Physics)*, 107, July 2002. doi: 10.1029/2001JA000237.
- [45] G. L. Siscoe, N. U. Crooker, and K. D. Siebert. Transpolar potential saturation: roles of region-1 current system and solar wind ram pressure. *J. Geophys. Res.*, 107(A10):1321, 2002. doi: 10.1029/2001JA009176.

- [46] G. L. Siscoe, G. M. Erickson, B. U. Ö. Sonnerup, N. C. Maynard, J. A. Schoendorf, K. D. Siebert, D. R. Weimer, W. W. White, and G. R. Wilson. Hill model of transpolar potential saturation: comparisons with MHD simulations. *J. Geophys. Res.*, 107(A6):1075, 2002. doi: 10.1029/2001JA000109.
- [47] E. J. Smith and J. H. Wolfe. Observations of interaction regions and corotating shocks between one and five AU - Pioneers 10 and 11. *GRL*, 3:137–140, March 1976. doi: 10.1029/GL003i003p00137.
- [48] E. Spencer, W. Horton, M. L. Mays, I. Doxas, and J. Kozyra. Analysis of the 3-7 October 2000 and 15-24 April 2002 geomagnetic storms with an optimized nonlinear dynamical model. *J. Geophys. Res.*, 112, April 2007. doi: 10.1029/2006JA012019.
- [49] E. Spencer, A. Rao, W. Horton, and M. L. Mays. Evaluation of solar wind-magnetosphere coupling functions during geomagnetic storms with the WINDMI model. *JGR*, 114:2206–+, February 2009. doi: 10.1029/2008JA013530.
- [50] E. C. Stone, A. M. Frandsen, R. A. Mewaldt, E. R. Christian, D. Margolies, J. F. Ormes, and F. Snow. The Advanced Composition Explorer. *Space Science Reviews*, 86:1–22, 1998.
- [51] M. Sugiura. Hourly values of equatorial Dst for the IGY. *Ann. Int. Geophys. Year*, 35(9):945, 1964.
- [52] M. Temerin and X. Li. A new model for the prediction of Dst on the basis

- of the solar wind. *Journal of Geophysical Research (Space Physics)*, 107:1472, December 2002. doi: 10.1029/2001JA007532.
- [53] M. Temerin and X. Li. Dst model for 1995-2002. *JGR*, 111(A10):4221, April 2006. doi: 10.1029/2005JA011257.
- [54] B. T. Tsurutani, W. D. Gonzalez, A. L. C. Gonzalez, F. L. Guarnieri, N. Gopalswamy, M. Grande, Y. Kamide, Y. Kasahara, G. Lu, I. Mann, R. McPherron, F. Soraas, and V. Vasyliunas. Corotating solar wind streams and recurrent geomagnetic activity: A review. *JGR*, 111:7–+, June 2006. doi: 10.1029/2005JA011273.
- [55] N. A. Tsyganenko and A. V. Usmanov. Determination of the Magnetospheric Current System Parameters and Development of Experimental Geomagnetic Field Models Based on Data from IMP and HEOS Satellites. *Planet. Space Sci.*, 30:985–98, 1982.
- [56] N. E. Turner, D. N. Baker, T. I. Pulkkinen, and R. L. McPherron. Evaluation of the tail current contribution to Dst. *J. Geophys. Res.*, 105:5431–5440, March 2000. doi: 10.1029/1999JA000248.
- [57] Y.M. Wang, P.Z. Ye, S. Wang, and X.H. Xue. An interplanetary cause of large geomagnetic storms: Fast forward shock overtaking preceding magnetic cloud. *Geophys. Res. Lett.*, 30(13), 2003. doi: 10.1029/2002GL016861.
- [58] J. A. Wanliss and K. M. Showalter. High-resolution global storm index: Dst versus SYM-H. *JGR*, 111:2202, February 2006. doi: 10.1029/2005JA011034.

- [59] D.R. Weimer, D.M. Ober, N.C. Maynard, M.R. Collier, D.J. McComas, N.F. Ness, C.W. Smith, and J. Watermann. Predicting Interplanetary magnetic field (IMF) propagation delay times using the minimum variance technique. *J. Geophys. Res.*, 108(A1):1026, 2003.
- [60] S. Yashiro, N. Gopalswamy, G. Michalek, O. C. St. Cyr, S. P. Plunkett, N. B. Rich, and R. A. Howard. A catalog of white light coronal mass ejections observed by the SOHO spacecraft. *J. Geophys. Res.*, 109, July 2004. doi: 10.1029/2003JA010282.
- [61] P.H. Yoon, A.T.Y. Lui, and M.I. Sitnov. Generalized lower-hybrid drift instabilities in current sheet equilibrium. *Phys. Plasmas*, 9(5):1526–1538, 2002.
- [62] X.-Y. Zhou, R. J. Strangeway, P. C. Anderson, D. G. Sibeck, B. T. Tsurutani, G. Haerendel, H. U. Frey, and J. K. Arballo. Shock aurora: FAST and DMSP observations. *J. Geophys. Res.*, 108:20, April 2003.
- [63] P. Zhu, W. Horton, and H. Sugama. The radial electric field in a tokamak with reversed magnetic shear. *Phys. Plasmas*, 6(6):2503, 1999.
- [64] T. H. Zurbuchen and I. G. Richardson. In-Situ Solar Wind and Magnetic Field Signatures of Interplanetary Coronal Mass Ejections. *Space Science Reviews*, September 2006. doi: 10.1007/s11214-006-9010-4.
- [65] T. H. Zurbuchen, G. Gloeckler, F. Ipavich, J. Raines, C. W. Smith, and L. A. Fisk. On the fast coronal mass ejections in October/November 2003: ACE-

SWICS results. *Geophys. Res. Lett.*, 31:L11805, June 2004. doi: 10.1029/
2004GL019461.

Vita

Mona Leila Mays was born in Baltimore, Maryland in 1982. She attended Tatbighi International School of Tehran and Behesht High School in Tehran, Iran and in 1999 she received a high school diploma in physics-mathematics as top student in her class. Upon graduating high school Leila went on to receive a B.S. with high honors in physics and astronomy from the University of Maryland College Park in 2004. Since August 2004 she has been pursuing a PhD in physics at the University of Texas at Austin with supervisor Wendell Horton and expects to finish in August 2009. After which she will begin a NASA Postdoctoral Program Fellowship with Dr. Chris St.Cyr at Goddard Space Flight Center. At Goddard Leila will continue her research in magnetospheric physics but specifically “Understanding Interplanetary Propagation and Resulting Geomagnetic Activity Using Modeling based on STEREO and THEMIS Observations.”

Permanent address: 1803 Rainy Meadows Dr, Austin, TX 78758

This dissertation was typeset with L^AT_EX[†] by the author.

[†]L^AT_EX is a document preparation system developed by Leslie Lamport as a special version of Donald Knuth’s T_EX Program.